Numerical Methods in Civil Engineering, 8-1 (2023) 79-101

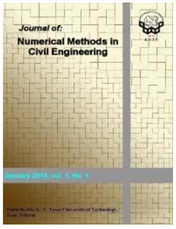

Numerical Methods in Civil Engineering

Journal Homepage: https://nmce.kntu.ac.ir/

The efficiency of Chisala's model in predicting the moment-rotation curve for double web angle, and welded flange plate connections

Nader Fanaie*, Mohammad Amin Moghaddasi, and Mehdi Fazli*****

ARTICLE INFO

RESEARCH PAPER

Article history:
Received:
March 2023.
Revised:
June 2023.
Accepted:
July 2023.

Keywords:
Chisala's model, Moment-rotation curve, double web angle, welded flange plate, finite element analysis

Abstract:

This research investigates the efficiency of Chisala's model in predicting the moment-rotation curve for double web angle and welded flange plate connections. As many types of connections of steel structures exhibit a semi-rigid (neither totally hinge, nor completely rigid) flexural performance, the determination of their moment-rotation curve is of vital importance since it provides a better vision for structural engineers. In this regard, analytical models of the types of connections mentioned in the title, with components of varying dimensions were created to derive the values of necessary parameters of Chisala's model. Using the obtained values, the moment-rotation curve for each type of connection was presented. As a means of verification, finite element analysis using Abaqus software was also carried out on each corresponding analytical model. A statistically derived relation, in terms of the parameters of Chisala's model, was then obtained, utilizing linear regression analysis, and was used afterward, to illustrate the moment-rotation curve for each type of connection. The comparison of moment rotation curves obtained both from analytical models and finite element analysis (FEA) suggest that Chisala's model is quite efficient and precise when used to illustrate the moment-rotation curve for double web angle and welded flange plate connections, and it can predict moment or rotation values, should the necessary parameters be obtained using a well-defined equivalent analytical model.

1. Introduction

In general, the performance of a structural element can be described in terms of its strength, stiffness, and ductility. The moment-rotation curve is an important indicator of the performance of connections, since the strength, stiffness, and ductility values can be derived from the curve, as shown in Figure 1.

There are many models proposed by researchers to present the moment-rotation curve of a steel connection which are described in upcoming sections.

1.1. Power models

In 1998, Richard et al. provided a power formula derived from an analytical model which is shown in Figure 2, to illustrate the moment-rotation curve for bolted double framing angle connections [1].

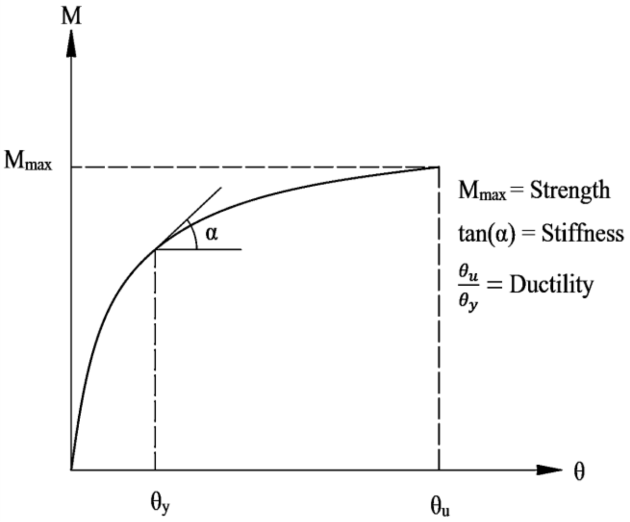

Fig. 1: The moment-rotation curve for a connection, and the relation between its parameters.

---

* *Associate Professor, Civil Engineering Department, K. N. Toosi University of Technology, Tehran, Iran. Email: fanaie@kntu.ac.ir.*

** *MSc, Civil Engineering Department, K. N. Toosi University of Technology, Tehran, Iran.*

*** *MSc, Fakoor Sanat Tehran Engineering Company, Tehran, Iran.*

https://doi.org/10.61186/NMCE.2303.1013

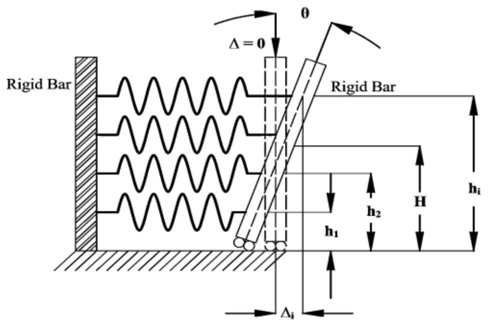

Fig. 2: Analytical model for double framing angles [1].

They compared the final results with the experimental work of Lewitt et al. [2] and the polynomial model proposed by Frye and Morris [3]. The results of this comparison suggest that the proposed power model is relatively precise for rotations larger than 0.003 radians [1]. Attiogbe and Morris used selected points and least-squares methods as curve-fitting procedures to determine the parameters of the Richard-Abbott [4], and Ramberg-Osgood [5] power models in 1991 [6]. They compared the two power models, and the results suggest that the Richard-Abbott formula has more precision [6]. Kishi et al. used the Ricard-Abbott power model to determine the moment-rotation relation for end-plate connections [7]. They carried out a total of 168 experiments on end-plate connections and used the obtained results to develop a moment-rotation formula [7]. In another verifying study, Abolmaali et al. used Richard-Abbott and Ramberg-Osgood power models to present moment-rotation curves for end-plate connections [8]. In 2020, Tran used the moment-rotation relation proposed by Kishi et al. and extended it for the moment-rotation curve of semi-rigid cruciform flush end-plate connections exposed to elevated temperatures [9].

1.2. Exponential models

In 1999, Chisala proposed the following three parameters exponential model and provided analytical models for three types of connections (double web angle, top and seat-angle, and double web angle with top and seat-angle) to be utilized to derive the parameters [10]:

$$M = \left[M_{\circ} + K_p\theta\right]\left[1 - exp(-K_i\theta/M_{\circ})\right] \tag{1}$$

where

M_0 = The intercept-constant [10]

K_i = The initial (elastic) stiffness of the connection [10]

K_p = The strain-hardening (plastic) stiffness of the connection [10]

The elastic (initial) stiffness (K_i), is the initial slope of the moment-rotation curve at zero. The plastic stiffness (K_p) is the slope of the same curve at the end of the plastic zone (before the failure of the connection). The intercept constant (M_0) on the other hand, controls the overall strength of the connection. All of the introduced parameters of Chisala's model are independent, which contributes to its efficiency. Using this model, Chisala solved many problems and difficulties generated by other models. Other exponential models were later developed by researchers including the work of Gilio et. al on cold-formed steel purlins with sleeved bolted connection [11], Zhou et al. introducing a two-parameter exponential relation [12], and a four-parameter exponential model developed by Zhao et al. [13].

1.3. Logarithmic models

In 2002, Lee and Moon proposed a two-parameter logarithmic model for semi-rigid connections with angles [14]. The main advantage of this model over others is that it has few parameters which can be determined easily. On disadvantages, the two parameters do not have any physical interpretation but this does not affect the calculations and results. Later in 2017, Kong and Kim developed an inverse hyperbolic model for top and seat-angle connections with double web angles which was verified by experiments [15]. The results of the comparison between analytical, and experimental data suggest that the proposed model has well-enough precision [15].

1.4. Three-linear model

In 2007, Danesh et al. developed a three-linear model for top and seat-angle connections with double web angles and obtained all of the parameters (M_p, M_y, K_n, K_t, K_i) shown in Figure 3 [16]:

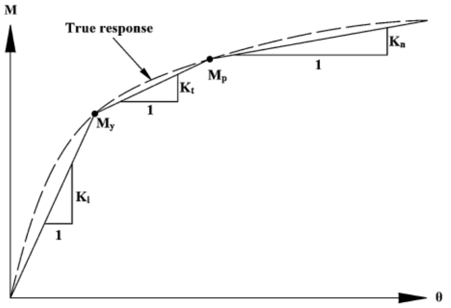

Fig. 3: Three-linear moment-rotation curve [16].

Where:

K_i = initial (elastic) stiffness of the connection [16]

K_n = normalized stiffness [16]

K_t = tangential stiffness [16]

M_p = plastic moment [16]

M_y = yield moment [16]

2. Materials

One of the important requirements of finite element analysis is the determination of material properties. Mofid et al. showed that a normalized sample stress-strain curve can be used for ordinary constructional steel [17]. The specifications of this particular curve are presented in Table 1.

Table 1: Specifications of stress-strain curve for different steel types [17].

Steel type	σ_y MPa	σ_u MPa	ε_y	ε_p	ε_h	ε_u	E MPa	E_h MPa	E_u MPa
S235	235	360	0.0011	0.0140	0.0370	0.1400	210000	5500	360
S275	275	430	0.0013	0.0150	0.0470	0.1200	210000	4800	430
S355	355	510	0.0017	0.0170	0.0530	0.1100	210000	4250	510
Constructional steel	σ_y	$1.5\ \sigma_y$	ε_y	$11\ \varepsilon_y$	$21\ \varepsilon_y$	$121\ \varepsilon_y$	E	E/20	E/500

Using the data available in Table 1, S235 was selected as main steel, and S355 was considered as weld steel. In this regard, the stress-strain curve for main steel and welds are presented in Figure 4.

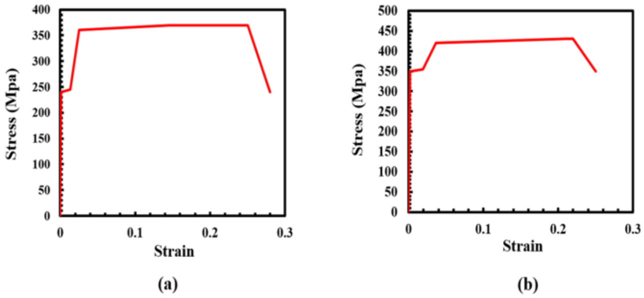

Fig. 4: Standard stress-strain curve (a) main steel (b) weld steel.

To verify the reliability of finite element modeling, test models were constructed, and the results were compared with experiments carried out by various researchers. In 2009, Ghobadi et al. tested 5 moment-resisting connection specimens under cyclic loading [18]. Among these 5 specimens, two were very close to welded flange plate connections proposed in this research. These two are RC2 (retrofitted connection), and RC4. The details of these two specimens are presented in Figure 5.

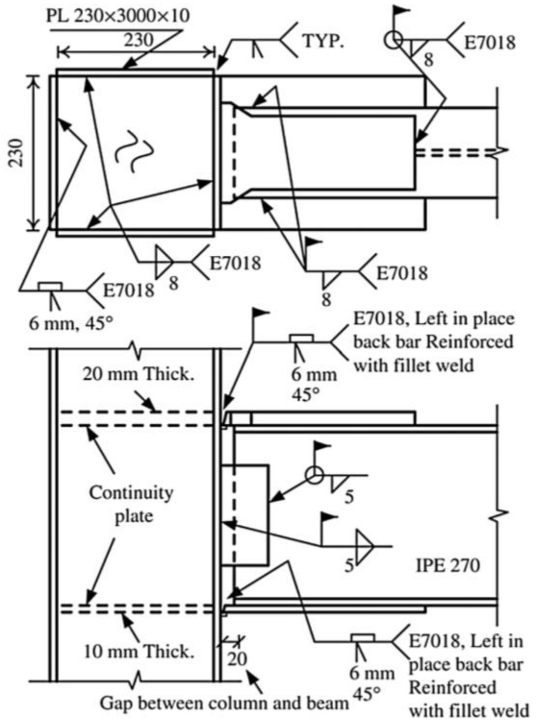

Fig. 5: Details of specimen RC2 [18].

The only difference between the two specimens (RC2, and RC4) is the type of bottom plate welds. The bottom plate is welded to the column using full penetration groove weld in RC2, and double-sided fillet weld in RC4. The test setup is shown in Figure 6.

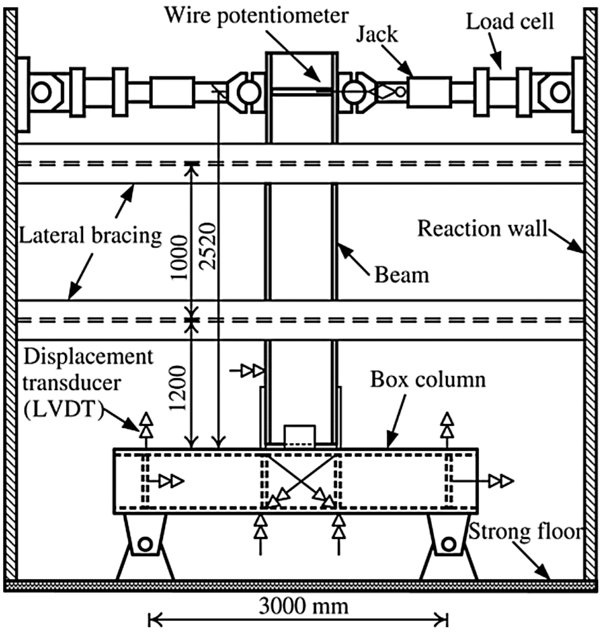

Fig. 6: Full-scale test setup [18].

The specimens are symmetric with respect to the beam web plane, therefore they were split in half, and a half was modeled. Elements C3D15 and C3D20 (of varying dimensions with hourglass control) were used to model the main steel, and the welds, respectively. The finite element model of the RC4 specimen is presented in Figure 7.

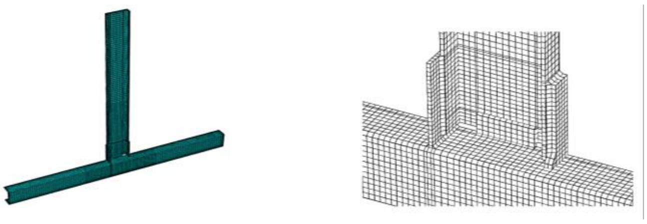

Fig. 7: Finite element model of specimen RC4.

Materials were selected according to the earlier discussion. The numerical and experimental moment-drift angle curves for each specimen are presented in Figure 8. and Figure 9. In these curves, the moment is normalized (M/M_p), where $M_p = Z\ .\ F_y$, and Z is the plastic section modulus of the beam, and the drift angle is calculated by dividing the relative horizontal beam deflection by its length.

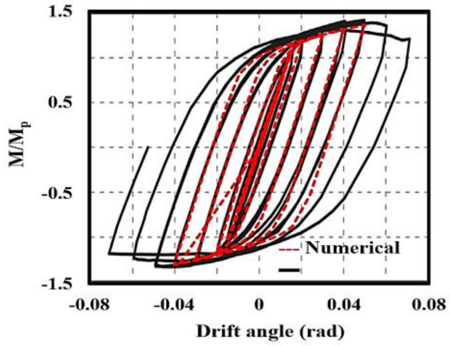

Fig. 8: Experimental [18] and numerical moment-drift angle curves for RC2 specimen.

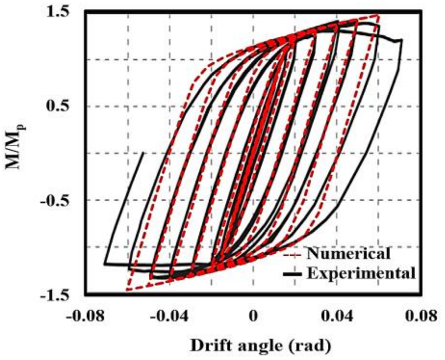

Fig. 9: Experimental [18] and numerical moment-drift angle curves for RC4 specimen.

3. Finite element models

3.1. Double web angle connection

The connection setup is presented in Figure 10.

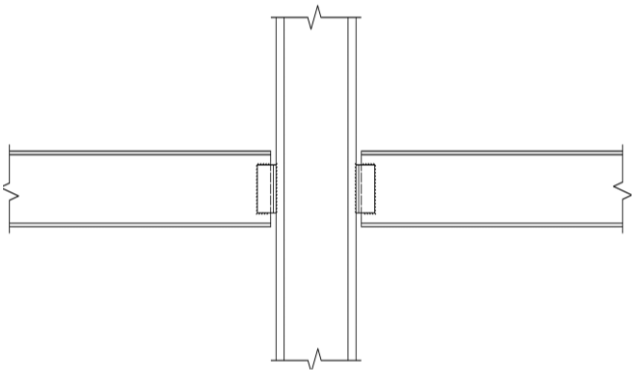

Fig. 10: Double web angle connection setup.

To determine the potential effects of geometric parameters on the performance of double web angle connections, a total of 35 specimens of the very kind of connection, were modeled and analyzed. Varying geometric parameters for all of the specimens are dimensions of the web angles. The details of each specimen are presented in Table 2.

Table 2: Details and dimensions of the finite element models of double web angle connection (DWA).

Specimen ID	Beam section	Column section	Web angles			Angles to beam weld leg length (mm)	Angles to column weld leg length (mm)
			Length (mm)	Flange width (mm)	Thickness (mm)		
DWA-01	IPE100 L=1000 mm	2IPE160	75	50	5	5	5
DWA-02					6		
DWA-03					7		
DWA-04			65				
DWA-05			55		7		7
DWA-06			75	60	6		6
DWA-07				70			
DWA-08	IPE140 L=1400 mm	2IPE220	90	60	5	5	5
DWA-09			100				
DWA-10			110				
DWA-11					8		
DWA-12					10		
DWA-13				80	8		
DWA-14				100			
DWA-15	IPE180 L=1800 mm	2IPE270	110	80	6	6	6
DWA-16			120				
DWA-17			130				
DWA-18					10		
DWA-19					12		
DWA-20				100			
DWA-21				120			
DWA-22	IPE220 L=2200 mm	2IPE270	140	80	6	6	6
DWA-23			150				
DWA-24			160				
DWA-25					10		
DWA-26					12		
DWA-27				100			
DWA-28				120			

DWA-29	IPE270 L=2700 mm	2IPE3000	160	100	8	8	8
DWA-30			170				
DWA-31			180				
DWA-32					12		
DWA-33					14		
DWA-34				120	12		
DWA-35				130			

The specimens are designed according to Eurocode 3 requirements [19]. A sample specimen is shown in Figure 11.

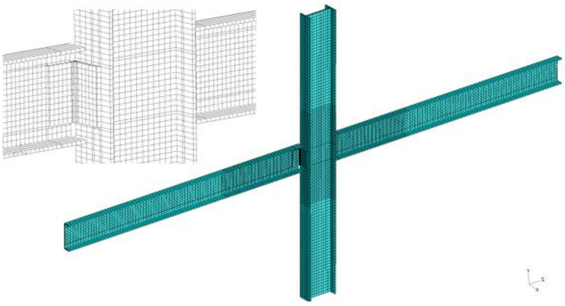

Fig. 11: Sample finite element model of double web angle connection.

The mesh was constructed using the C3D8 element for one-third of the lengths of beams and the column near the connection zone, the C3D20 element for angles, and the C3D15 element for welds.

3.2. *Welded flange plate connection*

The connection setup is shown in Figure 12.

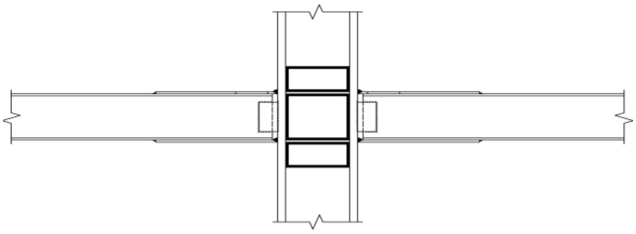

Fig. 12: Welded flange plate connection setup.

Similar to section 3.1, to determine the potential effects of geometric dimensions on the performance of the connection, a total of 78 specimens with varying dimensions were modeled and analyzed. The varying dimensions are thickness, length, and width of the top, bottom, and beam web stiffener plates, along with the thickness of doubler and continuity plates. The details of the specimens are presented in Table.

Table 3: Details and dimensions of the finite element models of moment-resisting connection designated as MR (dimensions are in millimeters).

Specimen ID	**Beam section**	**Column section**	**Top plate**					**Seat plate**	**Beam web stiffener**	**Doubler plate**	**Continuity plate**
			b$_1$	**b$_2$**	**L$_{t1}$**	**L**	**t**				
Top plate thickness											
MR-01	IPE180 L=2000 mm	2IPE200	60	80	60	200	15	200×120×8	110×80×6	400×180×6	180×40×6
MR-02							16				
MR-03							18				
MR-04							20				
MR-05	2IPE160 L=2000 mm	2IPE220	130	180	50	350	12	350×180×10	100×100×6	380×200×6	200×40×6
MR-06							15				
MR-07							16				
MR-08							18				
MR-09	2IPE200 L=2500 mm	2IPE270	170	230	60	400	15	400×220×10	130×130×6	420×245×6	245×50×6
MR-10							16				
MR-11							18				
MR-12							20				
Top plate length											
MR-01	IPE180 L=2000 mm	2IPE200	60	80	60	200	15	200×120×8	110×80×6	400×180×6	180×40×6
MR-13						230					
MR-14						260					
MR-15						290					
MR-05	2IPE160 L=2000 mm	2IPE220	130	180	50	350	12	350×180×10	100×100×6	380×200×6	200×40×6
MR-16					60						
MR-17					70						
MR-18					80						
MR-19	2IPE200 L=2500 mm	2IPE270	170	230	50	400	15	400×220×10	130×130×6	420×245×6	245×50×6
MR-20					55						
MR-09					60						
MR-21					65						
Top plate width											

MR-01	IPE180 L=2000 mm	2IPE200	60	80	60	200	15	200×120×8	110×80×6	400×180×6	180×40×6
MR-22			55								
MR-23			50								
MR-24			45								
MR-05	2IPE160 L=2000 mm	2IPE220	130	180	50	350	12	350×180×10	100×100×6	380×200×6	200×40×6
MR-25			135								
MR-26			140								
MR-27			145								
MR-09	2IPE200 L=2500 mm	2IPE270	170	230	50	400	15	400×220×10	130×130×6	420×245×6	245×50×6
MR-28			175								
MR-29			180								
MR-30			185								
Bottom plate thickness											
MR-01	IPE180 L=2000 mm	2IPE200	60	80	60	200	15	200×120×8	110×80×6	400×180×6	180×40×6
MR-31								200×120×10			
MR-32								200×120×12			
MR-33								200×120×15			
MR-05	2IPE160 L=2000 mm	2IPE220	130	180	50	350	12	350×180×10	100×100×6	380×200×6	200×40×6
MR-34								350×180×12			
MR-35								350×180×15			
MR-36								350×180×16			
MR-09	2IPE200 L=2500 mm	2IPE270	170	230	50	400	15	400×220×10	130×130×6	420×245×6	245×50×6
MR-37								400×220×12			
MR-38								400×220×15			
MR-39								400×220×16			
Bottom plate length											
MR-01	IPE180 L=2000 mm	2IPE200	60	80	60	200	15	200×120×8	110×80×6	400×180×6	180×40×6
MR-40								230×120×8			
MR-41								260×120×8			
MR-42								290×120×8			
Bottom plate width											
MR-01	IPE180 L=2000 mm	2IPE200	60	80	60	200	15	200×120×8	110×80×6	400×180×6	180×40×6
MR-43								200×130×8			
MR-44								200×140×8			
MR-45								200×150×8			
MR-05	2IPE160 L=2000 mm	2IPE220	130	180	50	350	12	350×180×10	100×100×6	380×200×6	200×40×6
MR-46								350×185×10			
MR-47								350×190×10			
MR-48								350×195×10			
MR-09	2IPE200 L=2500 mm	2IPE270	170	230	50	400	15	400×220×10	130×130×6	420×245×6	245×50×6
MR-49								400×225×10			
MR-50								400×230×10			
MR-51								400×235×10			
Beam web stiffener thickness											
MR-01	IPE180 L=2000 mm	2IPE200	60	80	60	200	15	200×120×8	110×80×6	400×180×6	180×40×6
MR-52									110×80×8		
MR-53									110×80×10		
MR-54									110×80×12		
Beam web stiffener length											
MR-55	IPE180 L=2000 mm	2IPE200	60	80	60	200	15	200×120×8	120×80×6	400×180×6	180×40×6
MR-01									110×80×6		
MR-56									100×80×6		
MR-57									90×80×6		
Beam web stiffener width											
MR-58	IPE180 L=2000 mm	2IPE200	60	80	60	200	15	200×120×8	110×90×6	400×180×6	180×40×6
MR-01									110×80×6		
MR-59									110×70×6		
MR-60									110×60×6		
Continuity plate thickness											

MR-01	IPE180 L=2000 mm	2IPE200	60	80	60	200	15	200×120×8	110×80×6	400×180×6	180×40×6
MR-61											180×40×8
MR-62											180×40×10
MR-63											180×40×12
MR-05	2IPE160 L=2000 mm	2IPE220	130	180	50	350	12	350×180×10	100×100×6	380×200×6	200×40×6
MR-64											200×40×8
MR-65											200×40×10
MR-66											200×40×12
MR-09	2IPE200 L=2500 mm	2IPE270	170	230	50	400	15	400×220×10	130×130×6	420×245×6	245×50×6
MR-67											245×50×8
MR-68											245×50×10
MR-69											245×50×12
Doubler plates thickness											
MR-01	IPE180 L=2000 mm	2IPE200	60	80	60	200	15	200×120×8	110×80×6	400×180×6	180×40×6
MR-70										400×180×8	
MR-71										400×180×10	
MR-72										400×180×12	
MR-05	2IPE160 L=2000 mm	2IPE220	130	180	50	350	12	350×180×10	100×100×6	380×200×6	200×40×6
MR-73										380×200×8	
MR-74										380×200×10	
MR-75										380×200×12	
MR-09	2IPE200 L=2500 mm	2IPE270	170	230	50	400	15	400×220×10	130×130×6	420×245×6	245×50×6
MR-76										420×245×8	
MR-77										420×245×10	
MR-78										420×245×12	

All specimens were designed according to Eurocode 3 [19]. A sample specimen is presented in Figure 13.

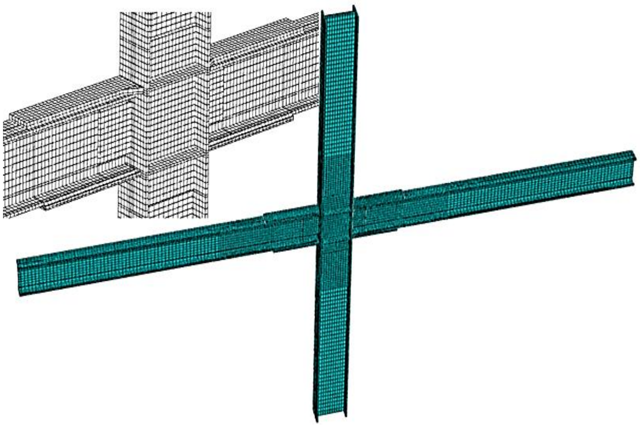

Fig. 13: A sample finite element model of welded flange plate connection.

Meshing was done using the same elements described in section 3.1.

4. Analytical models

4.1. Double web angle connection

Yang and Lee calculated the initial stiffness of double web angle connections using the theory of plates and shells [20]. They utilized an equivalent plate instead of web angles. The boundary conditions of the plate are assumed as a simple edge at the contact zone between the angle section and the column, a clamped edge at the angle-column weld, and two free edges [20]. Figure 14. depicts the proposed plate model.

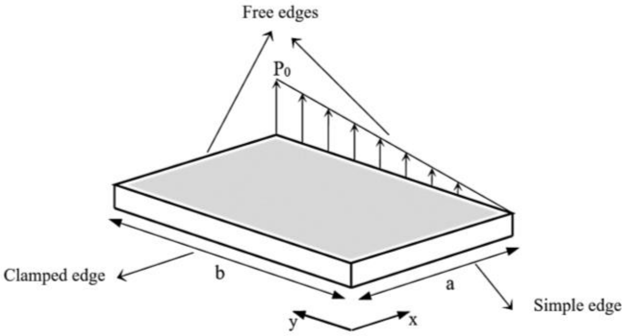

Fig. 14: Yang et al. model for calculating the initial stiffness [20].

The displacement for the proposed plate model is assumed as:

$$W(x,y) = \bar{w}x^2y \tag{2}$$

The following are the boundary conditions that are satisfied perfectly by Equation (2).

$$\begin{aligned} W(0,y) &= 0, \frac{\partial W(0,y)}{\partial x} = 0 \\ W(x,0) &= 0, \frac{\partial W^2(x,0)}{\partial y^2} = 0 \end{aligned} \tag{3}$$

The strain energy of the plate under flexure is:

$$U = \frac{1}{2}\int_0^a \int_0^b D\left\{\left(\frac{\partial^2 w}{\partial x^2} + \frac{\partial^2 w}{\partial y^2}\right)^2 - 2(1-\nu)\left[\frac{\partial^2 w}{\partial x^2}\frac{\partial^2 w}{\partial y^2} - \left(\frac{\partial^2 w}{\partial x \partial y}\right)^2\right]\right\} dydx \tag{4}$$

By substitution of Equation (2) into Equation (4), we get:

$$U = \frac{2}{3} D\bar{w}^2 ab(b^2 + 2(1-\nu)a^2) \tag{5}$$

Also, the potential energy of external forces is:

$$V_p = -\int_0^a \int_0^b P(x,y).W(x,y)dydx \tag{6}$$

Substitution of Equation (2) into Equation (6), yields:

$$V_p = -\frac{1}{3}\bar{w}P_0 a^2 b^2 \tag{7}$$

The total potential energy function becomes:

$$\Pi = U + V_p = \frac{2}{3}D\bar{w}^2 ab(b^2 + 2(1-\nu)a^2) - \frac{1}{3}\bar{w}P_0 a^2 b^2 \tag{8}$$

Using the Ritz method [20, 21], $\bar{w}$ can be obtained:

$$\frac{\partial \Pi}{\partial \bar{w}} = 0 \Rightarrow \bar{w} = \frac{P_0 ab}{4D(b^2+2(1-\nu)a^2)} \tag{9}$$

The rotational stiffness of single angle section is:

$$\theta = tan^{-1}\left(\frac{W(a,b)}{b}\right) \cong \frac{P_0 a^3 b}{4D(b^2+2(1-\nu)a^2)} \tag{10}$$

$$K_i' = \frac{M_0}{\theta} = \frac{4Db\left(b^2+2(1-\nu)a^2\right)}{3a^3} \tag{11}$$

Knowing that $D = Et^3/\left(12(1-\nu^2)\right)$ the initial stiffness of double web angle connection becomes:

$$K_i = \frac{2bEt^3(b^2+2(1-\nu)a^2)}{9a^3(1-\nu^2)} \tag{12}$$

Using the above equation to determine the actual value of the initial stiffness of a double web angle connection, and comparing the outcome with FEA results, reveals its major flaw. Yang et al. assumed that the rotation axis about the lower flange of the angle section [20], but changes in dimension of the angle section will change the location of the rotation axis. To solve this issue the length of the angle section (*b*) should be reduced to its actual value (b_{eff}). As discussed, the location of the rotation axis is a function of the dimensions of the angle section, which can be described by the following relation:

$$b_{eff} = a_1(b)^{a_2}(t)^{a_3}(a)^{a_4} \tag{13}$$

Where *t* is thickness, a_1 is a constant, a_2, a_3, and a_4 are dimensionless powers indicating the effect of each geometric parameter, and *a* is obtained using the relation below:

$$a = L - 2a_w - t - r \tag{14}$$

In the above relation, *L* is angle flange length, a_w is fillet weld leg, and *r* is fillet radius of the angle section.

To determine the values of a_1 to a_4, a linear regression analysis was carried out. Natural logarithm was applied on both sides of the Equation (13), to obtain a linear relation, which yields:

$$ln(b_{eff}) = ln(a_1) + a_2\, ln(b) + a_3\, ln(t) + a_4\, ln(L) \tag{15}$$

According to the results of the regression analysis, the effective length of the angle section (b_{eff}) can be calculated as follows:

$$b_{eff} = 0.54b(a)^{0.34}(t)^{-0.44} \tag{16}$$

All of the parameters above are measured in millimeters. At last, the elastic stiffness can be obtained by substitution of Equation (16) into Equation (12):

$$K_i = \frac{2b_{eff}Et^3(b_{eff} + 2(1-\nu)a^2)}{9a^3(1-\nu^2)} \tag{17}$$

Plastic stiffness is usually assumed in terms of elastic stiffness. In this regard, Equation (18) is proposed:

$$K_p = b_1(K_i)^{b_2} \tag{18}$$

Using regression analysis b_1, and b_2 are obtained, the results of which are presented in Figure 15.

$$K_p = 0.072K_i \tag{19}$$

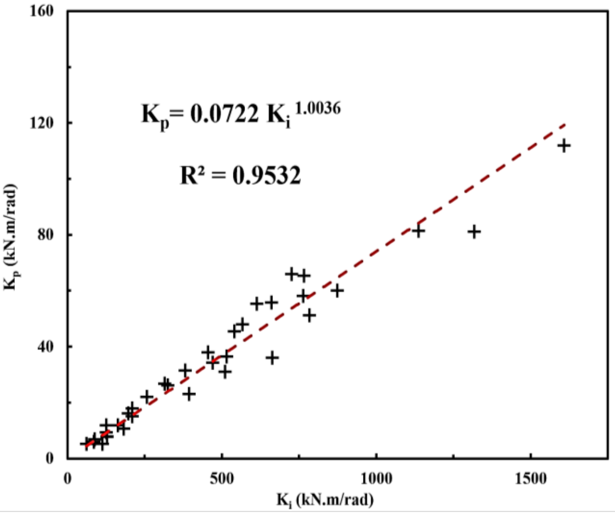

Fig. 15: Results of regression analysis on constants of plastic stiffness.

The intercept constant, being the last parameter of Chisala's model, can be described as the following:

$$M_0 = c_1(b_{eff})^{c_2}(a)^{c_3}(t)^{c_4} \tag{20}$$

Similar to previous equations, linear regression analysis was used to determine the unknown constant, and power values, which yields:

$$M_o = 334 \times 10^{-6}(b_{eff})^{1.81}(a)^{-0.97}(t)^{2.2} \tag{21}$$

In Equation (21), b_{eff}, *a*, and *t* are in millimeters, while M_o is in kilo-Newtons meters (*kN. m*).

4.2. Welded flange plate connection

To determine the parameters of Chisala's model, an equivalent spring system was constructed, which is presented in Figure 16.

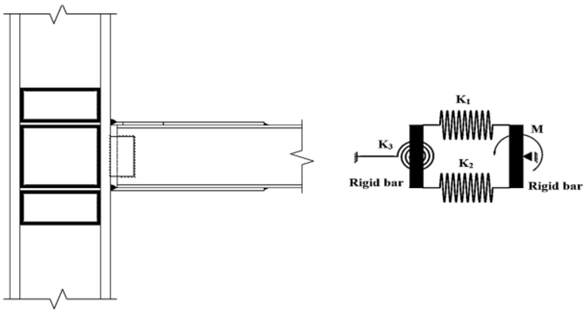

Fig. 16: The analytical spring system model of welded flange plate connection.

In Figure 16, K_1, K_2, and K_3 are axial stiffness of the top plate, axial stiffness of the bottom plate, and rotational stiffness of the panel zone, respectively. Finite element analysis suggests that increasing the length of the welded zone of the top plate (L_{t1}) does not significantly affect the performance of the connection. But as it is depicted in Figure 17., an equally long free zone (unwelded to the flange of the beam) will deform, and exhibit strains.

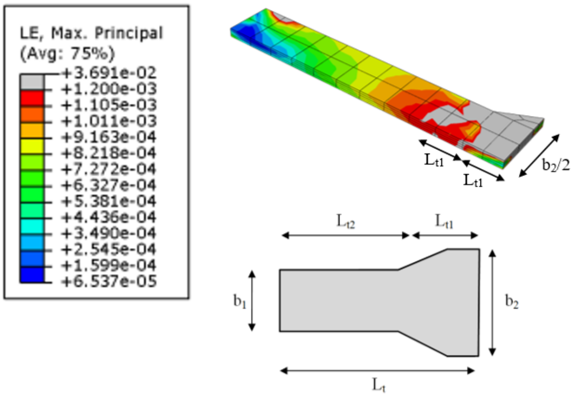

Fig. 17: Strain distribution on the top plate.

According to Figure 17., the axial stiffness of the top plate can be written as:

$$\Delta_t = \int_0^{2L_{t1}} \frac{P_t dx}{EA_t(x)} = \int_0^{L_{t1}} \frac{P_t dx}{Eb_t t_t} + \int_L^{2L_{t1}} \frac{P_t dx}{Et_t[x(b_2-b_1)+L(2b_1-b_2)]} = \frac{P_t L_{t1}}{Et_t} + \frac{P_t L_{t1} \ln(b_2/b_1)}{Et_t(b_2-b_1)}$$

$$K_1 = \frac{P_t}{\Delta_t} = \frac{Et_t(b_1-b_2)}{L_{t1}[1-(b_2/b_1)-\ln(b_2/b_1)]} \tag{22}$$

For the bottom plate, the same assumptions can be made, as presented in Figure 18.

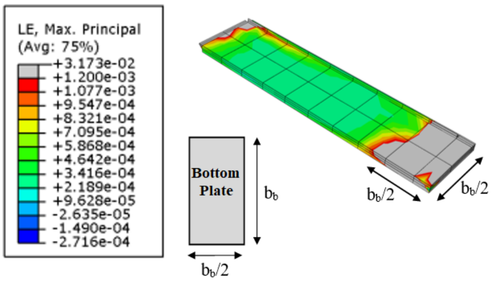

Fig. 18: Strain distribution in the bottom plate.

The axial stiffness of the bottom plate is:

$$K_2 = \frac{EA_b}{L_b}\frac{Eb_b t_b}{(b_b/2)} = 2Et_b \tag{23}$$

A common method of calculating the rotational stiffness of the panel zone is transforming all of the forces acting on it, to an equivalent shear force, and calculating pure shear deformations [22, 23]. This transformation is presented in Figure 19.

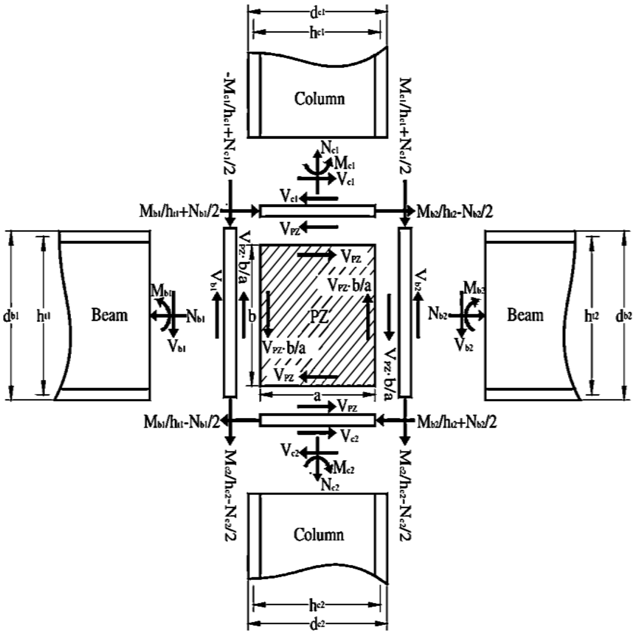

Fig. 19: Forces acting on the panel zone [23].

Horizontal equilibrium equations will yield:

$$V_{pz} = \frac{M_{b1}}{h_{b1}} + \frac{M_{b2}}{h_{b2}} - V_{c1} \tag{24}$$

The total equilibrium of the panel zone results in:

$$V_{c1} = V_{c2} \tag{25}$$

If it is assumed that the height of the column (H) is equal to the average of the heights on both sides of the panel zone, the equality of the shear forces leads to:

$$\left.\begin{aligned} V_{c1} &= \frac{2M_{c1}}{H-h_b} \\ V_{c2} &= \frac{2M_{c2}}{H-h_b} \end{aligned}\right\} \xrightarrow{V_{c1}=V_{c2}} M_{c1} = M_{c2} \tag{26}$$

Writing the moment equilibrium equation for the whole panel zone outputs:

$$M_{b1} + M_{b2} = M_{c1} + M_{c2} = 2M_{c1} \tag{27}$$

Finally, the shearing force of the panel zone becomes:

$$\begin{aligned} V_{pz} &= \frac{M_{b1}}{h_{b1}} + \frac{M_{b2}}{h_{b2}} - \frac{2M_{c1}}{H-h_b} \\ &\cong \frac{M_{b1}+M_{b2}}{h_b}(1-\rho) \\ \rho &= \frac{h_b}{H-h_b} \end{aligned} \tag{28}$$

To calculate the rotational stiffness of the panel zone, the following equations are employed:

$$\tau = G\gamma \tag{29}$$

$$V_{pz} = GA\gamma \tag{30}$$

Substituting Equation (28) into Equation (30) and considering that $M_{b1} + M_{b2} = M$, yields:

$$M = \frac{GAh_b}{1-p}\gamma \tag{31}$$

Therefore, the rotational stiffness of the panel zone is equal to:

$$K_3 = \frac{G(h_c - 2t_{fc})(t_{wc} + t_{pz})h_b}{1-p} \tag{32}$$

At last, the initial stiffness of the welded flange plate connection can be calculated using the following equation:

$$K_i = \frac{K_1K_2K_3h_b^2}{(K_1+K_2)K_3 + K_1K_2h_b^2} \tag{33}$$

Similar to the previous section, the plastic stiffness of the connection can be written in terms of the initial stiffness. Using regression analysis, the following equation is produced:

$$K_p = 0.1548(K_i)^{0.83} \tag{34}$$

Results of the regression analysis are presented in Figure 20.

Using all the obtained equations along with another regression analysis, the intercept constant for welded flange plate connections becomes:

$$M_0 = 522.4 \times 10^{-6}\left(\frac{b_1 + b_2}{2}\right)^{0.49} t_t^{0.22} L_{t1}^{\;-0.06} b_b^{0.27} t_b^{0.14} t_p^{0.028} (t_{cw} + t_{pz})^{0.18} h_b^{1.34} \tag{35}$$

5. Results and discussion

5.1. *Double web angle connection*

The calculation results using analytical, and finite element models, are presented in Table 4.

As it appears, Chisala's model can precisely determine the values needed to construct the moment-rotation curve for double web angle connections. Based on the obtained data, analytical and numerical moment-rotation curves for each specimen were illustrated. These curves are presented in the figures 21 to 52:

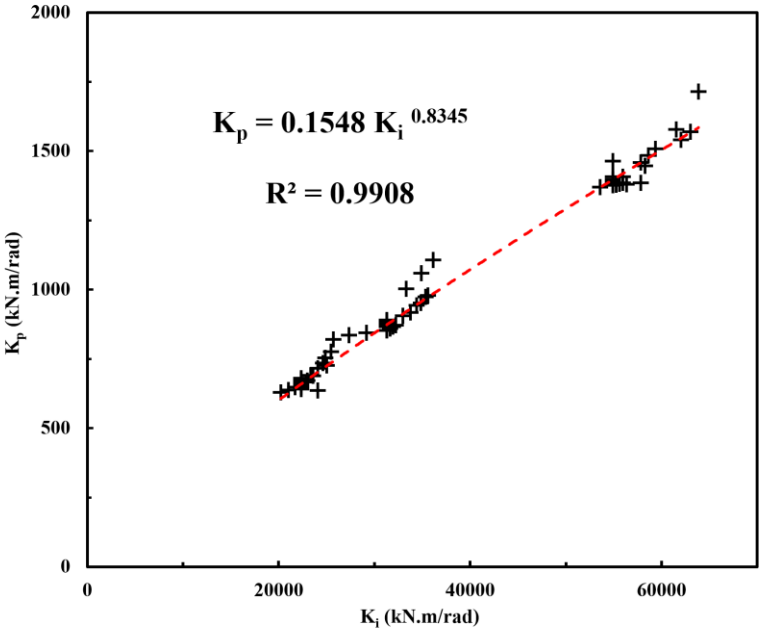

Fig. 20: Results of the regression analysis to determine the plastic stiffness.

Table 4: Analytical and numerical results for double web angle connection.

Specimen ID.	**K_i (kN.m/rad)**		**K_p (kN.m/rad)**		**M_0 (kN.m)**	
	(Analytical)	**(Abaqus)**	**(Analytical)**	**(Abaqus)**	**(Analytical)**	**(Abaqus)**
DWA-01	84.900	80.600	6.100	6.000	0.800	0.760
DWA-02	127.600	128.100	9.200	7.900	1.040	1.050
DWA-03	181.800	186.100	13.100	10.700	1.310	1.370
DWA-04	128.100	133.300	9.200	7.700	1.010	1.080
DWA-05	112.500	117.000	8.100	7.600	0.790	0.90
DWA-06	87.800	92.100	6.300	6.900	0.960	1.010
DWA-07	61.000	62.600	4.400	5.300	0.880	0.850
DWA-08	124.900	132.500	9.000	9.300	1.310	1.330
DWA-09	163.300	165.600	11.800	11.900	1.580	1.570
DWA-10	209.500	197.600	15.100	15.100	1.880	1.850

DWA-11	393.700	371.500	28.300	23.000	2.880	2.650
DWA-12	663.200	577.200	47.800	36.100	4.020	3.600
DWA-13	196.300	203.600	14.100	16.200	2.480	2.530
DWA-14	125.400	125.500	9.000	11.900	2.230	2.200
DWA-15	208.900	235.900	15.000	17.900	2.510	2.730
DWA-16	257.500	282.500	18.500	22.000	2.930	3.100
DWA-17	314.700	333.400	22.700	26.800	3.390	3.530
DWA-18	515.300	557.400	37.100	36.500	4.710	4.900
DWA-19	783.400	837.800	56.400	51.200	6.180	6.400
DWA-20	469.600	506.100	33.800	34.300	5.490	5.700
DWA-21	324.800	323.400	23.400	26.100	5.010	5.000
DWA-22	380.500	403.000	27.400	31.500	3.880	4.050
DWA-23	455.500	467.600	32.800	38.000	4.400	4.450
DWA-24	540.400	536.500	38.900	45.500	4.950	5.000
DWA-25	874.000	896.900	62.900	60.000	6.860	6.870
DWA-26	1317.700	1344.200	94.900	81.100	8.990	8.900
DWA-27	763.800	804.900	55.000	58.200	8.000	8.000
DWA-28	510.200	477.800	36.700	39.800	7.300	6.250
DWA-29	566.500	634.900	40.800	48.000	6.260	6.600
DWA-30	660.500	723.700	47.600	55.800	6.990	7.300
DWA-31	765.200	817.300	55.100	65.300	7.750	7.900
DWA-32	1136.300	1234.200	81.800	81.500	10.130	10.400
DWA-33	1608.300	1719.300	115.800	112.000	12.720	13.000
DWA-34	725.300	722.300	52.200	65.900	9.190	9.350
DWA-35	612.600	594.000	44.100	55.400	8.850	9.000

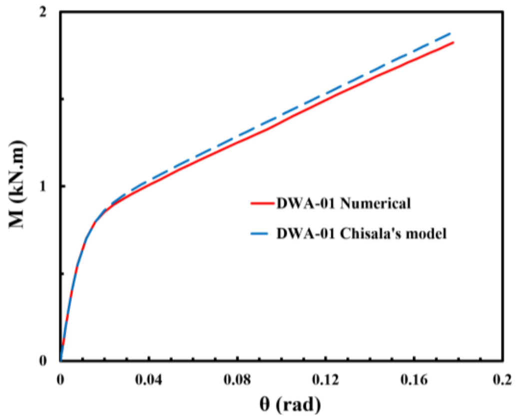

Fig. 21: Numerical and analytical moment-rotation curves for DWA-01 specimen.

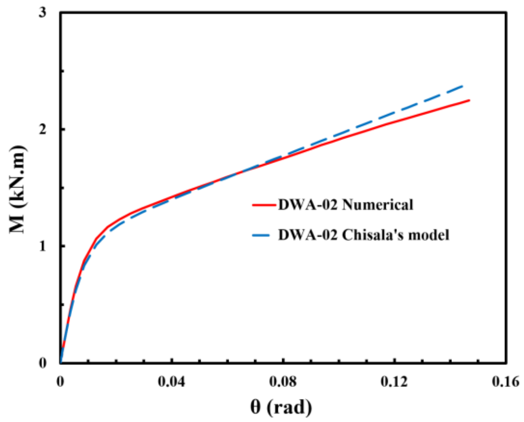

Fig. 22: Numerical and analytical moment-rotation curves for DWA-02 specimen.

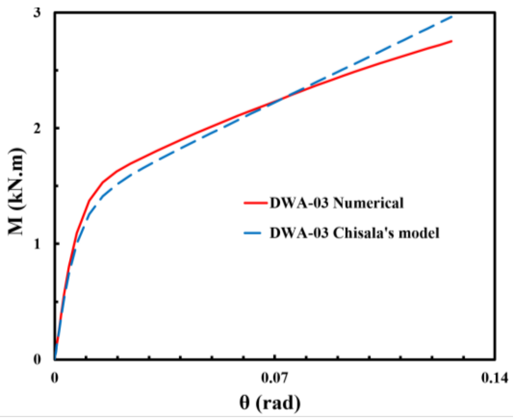

Fig. 23: Numerical and analytical moment-rotation curves for DWA-03 specimen.

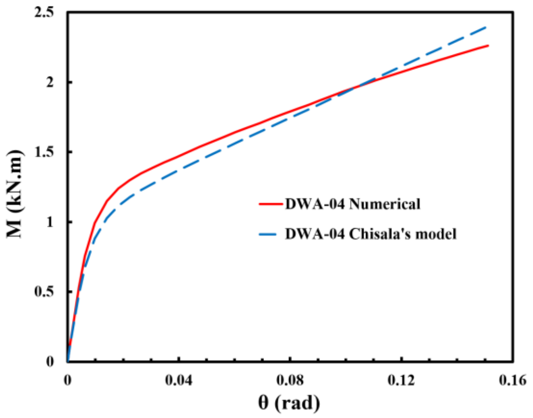

Fig. 24: Numerical and analytical moment-rotation curves for DWA-04 specimen.

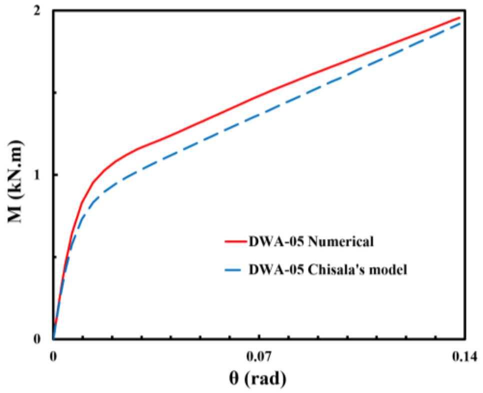

Fig. 25: Numerical and analytical moment-rotation curves for DWA-05 specimen.

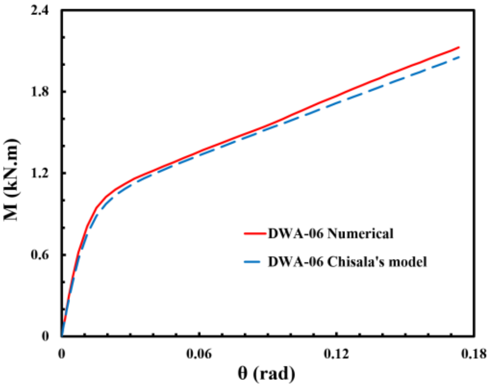

Fig. 26: Numerical and analytical moment-rotation curves for DWA-06 specimen.

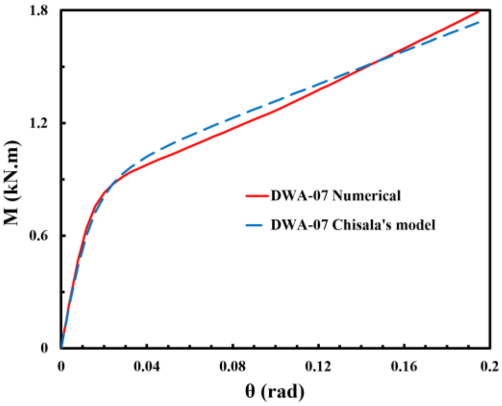

Fig. 27: Numerical and analytical moment-rotation curves for DWA-07 specimen.

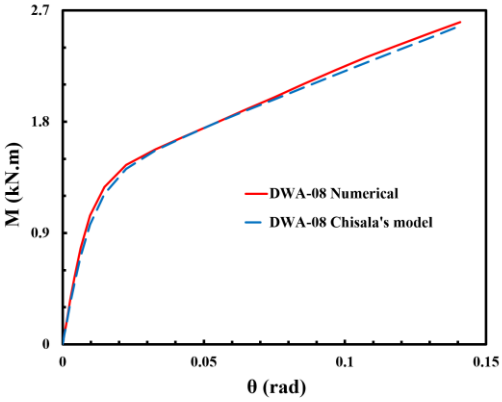

Fig. 28: Numerical and analytical moment-rotation curves for DWA-08 specimen.

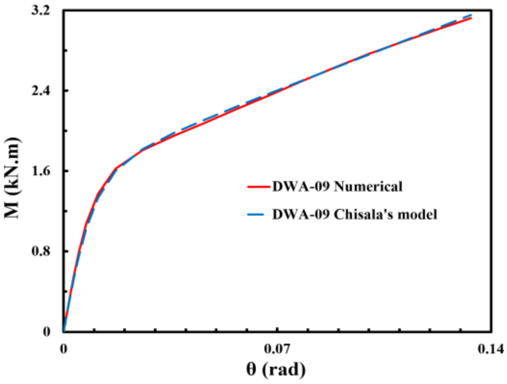

Fig. 29: Numerical and analytical moment-rotation curves for DWA-09 specimen.

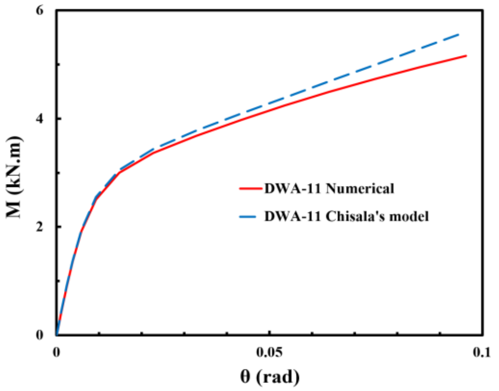

Fig. 30: Numerical and analytical moment-rotation curves for DWA-11 specimen.

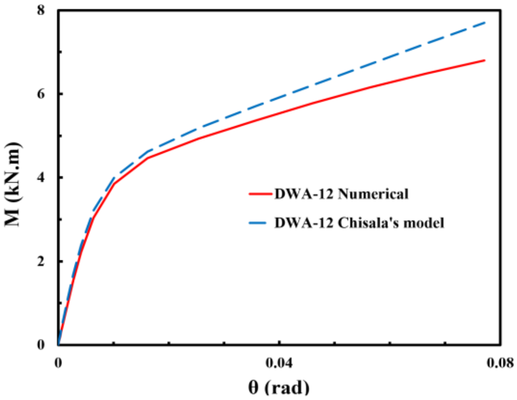

Fig. 31: Numerical and analytical moment-rotation curves for DWA-12 specimen.

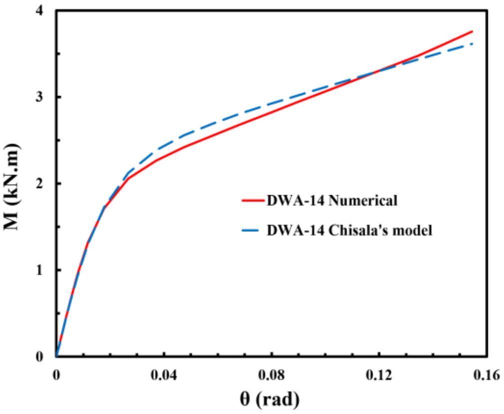

Fig. 32: Numerical and analytical moment-rotation curves for DWA-14 specimen.

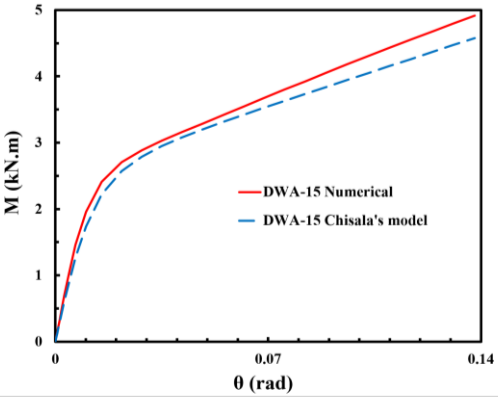

Fig. 33: Numerical and analytical moment-rotation curves for DWA-15 specimen.

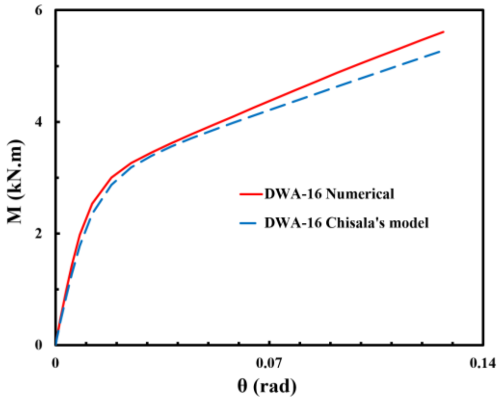

Fig. 34: Numerical and analytical moment-rotation curves for DWA-16 specimen.

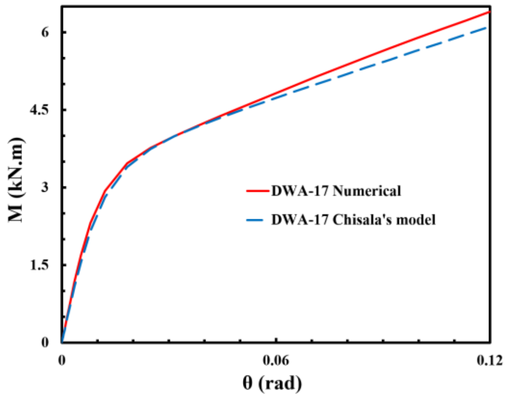

Fig. 35: Numerical and analytical moment-rotation curves for DWA-17 specimen.

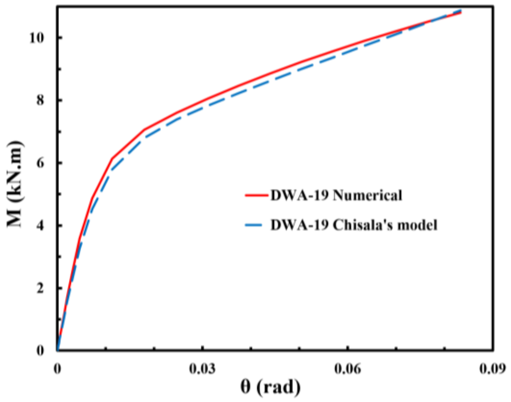

Fig. 36: Numerical and analytical moment-rotation curves for DWA-19 specimen.

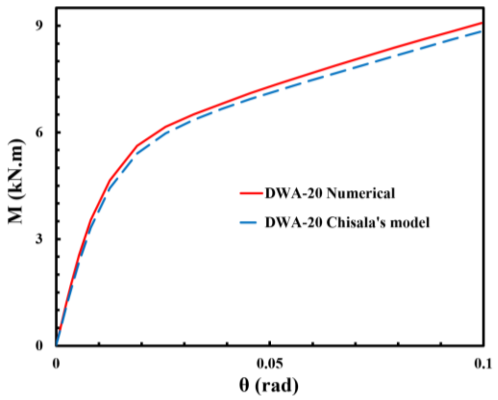

Fig. 37: Numerical and analytical moment-rotation curves for DWA-20 specimen.

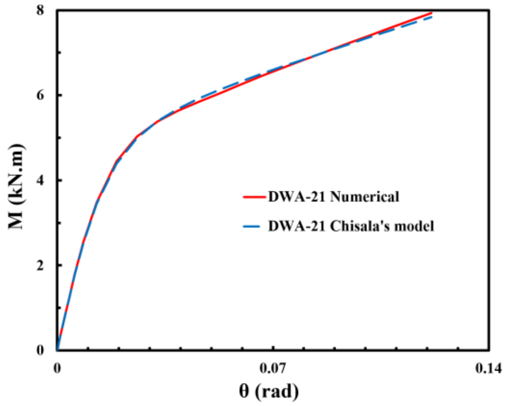

Fig. 38: Numerical and analytical moment-rotation curves for DWA-21 specimen.

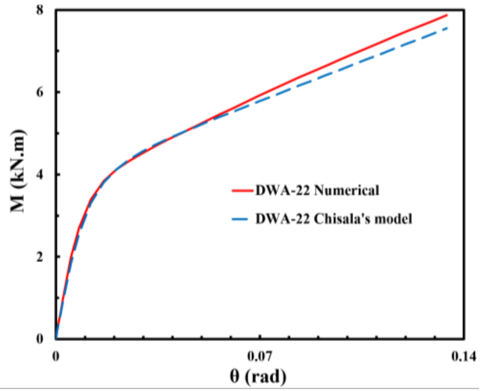

Fig. 39: Numerical and analytical moment-rotation curves for DWA-22 specimen.

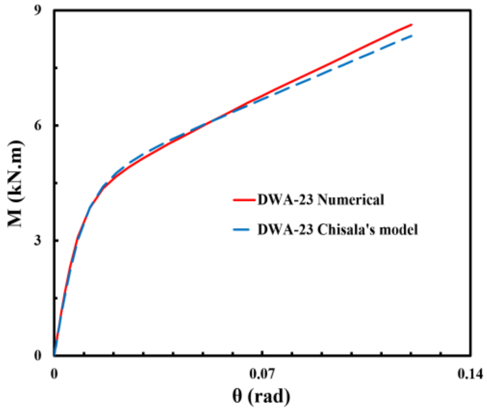

Fig. 40: Numerical and analytical moment-rotation curves for DWA-23 specimen.

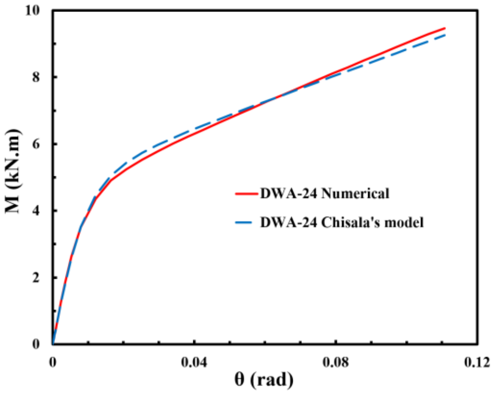

Fig. 41: Numerical and analytical moment-rotation curves for DWA-24 specimen.

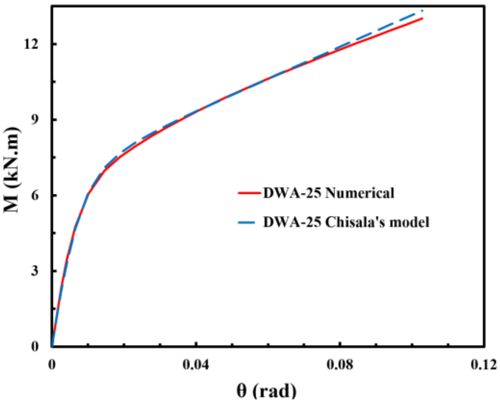

Fig. 42: Numerical and analytical moment-rotation curves for DWA-25 specimen.

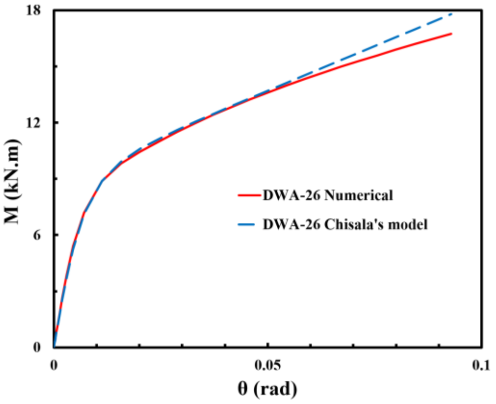

Fig. 43: Numerical and analytical moment-rotation curves for DWA-26 specimen.

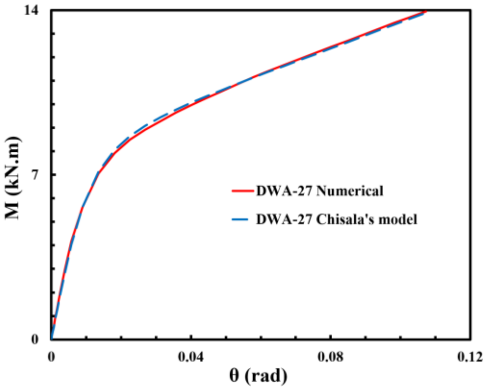

Fig. 44: Numerical and analytical moment-rotation curves for DWA-27 specimen.

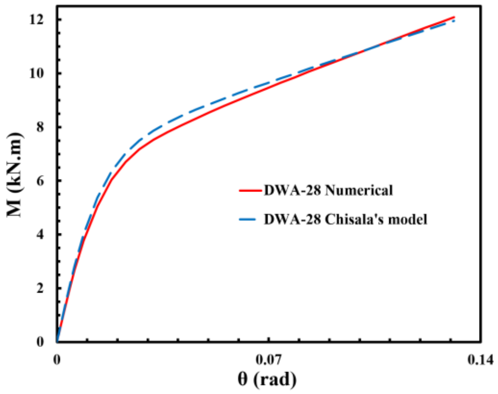

Fig. 45: Numerical and analytical moment-rotation curves for DWA-28 specimen.

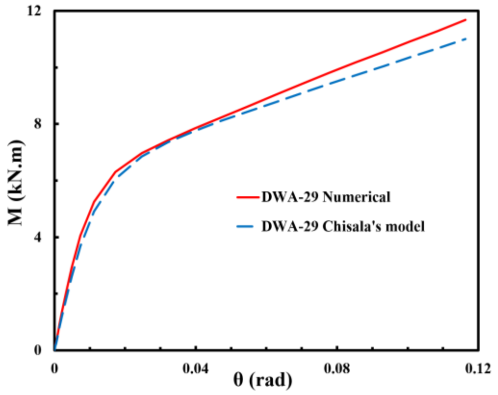

Fig. 46: Numerical and analytical moment-rotation curves for DWA-29 specimen.

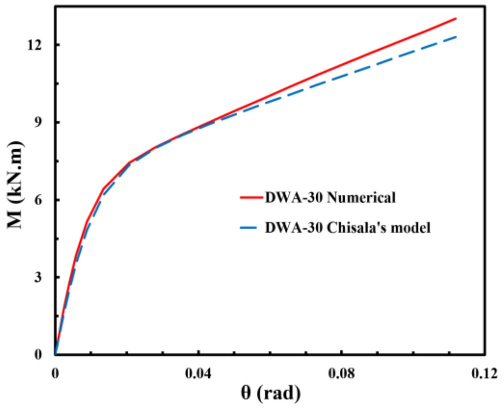

Fig. 47: Numerical and analytical moment-rotation curves for DWA-30 specimen.

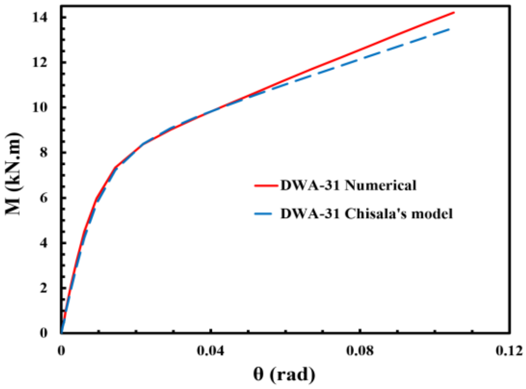

Fig. 48: Numerical and analytical moment-rotation curves for DWA-31 specimen.

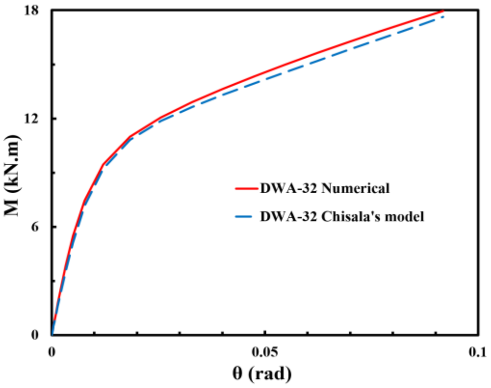

Fig. 49: Numerical and analytical moment-rotation curves for DWA-32 specimen.

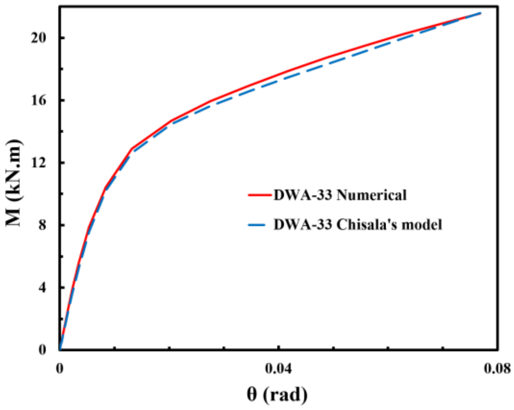

Fig. 50: Numerical and analytical moment-rotation curves for DWA-33 specimen.

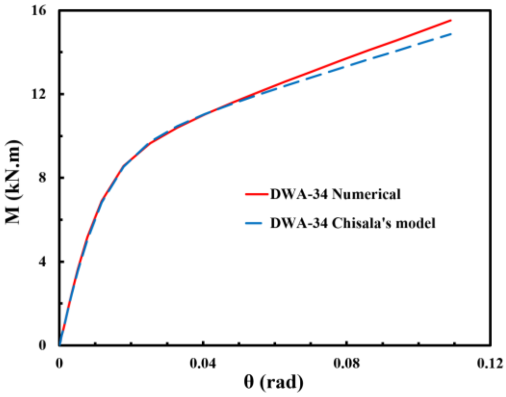

Fig. 51: Numerical and analytical moment-rotation curves for DWA-34 specimen.

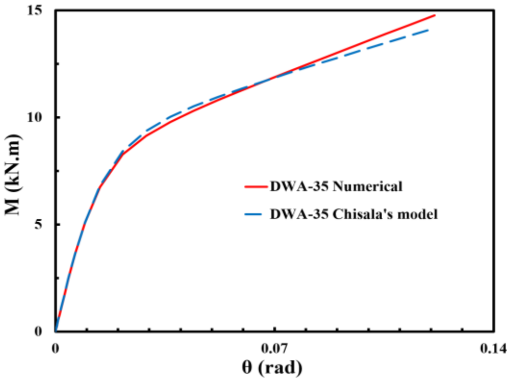

Fig. 52: Numerical and analytical moment-rotation curves for DWA-35 specimen.

Of course, some other results and conclusions can be derived from this comparison (analytical versus numerical), which are described in the following sections.

5.1.1. *Effects of web angle thickness*

Based on the results, it was observed that a slight increase of web angle thickness, significantly increases the elastic stiffness, plastic stiffness, and total strength of the connection. For instance, comparing specimens DWA-10, and DWA-11 reveals that changing web angle thickness from 6mm to 8mm increases the initial stiffness by 88%, and the plastic stiffness by 52%, as presented in Figure 53.

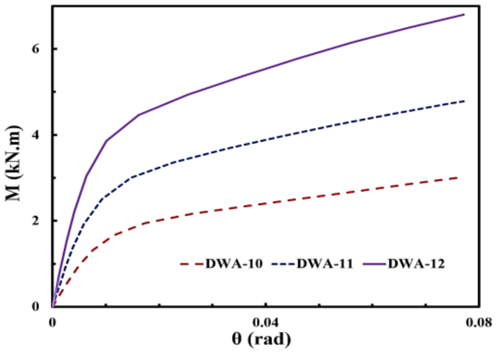

Fig. 53: Effects of web angle thickness on the performance of the connection.

5.1.2. *Effects of web angle length*

The web angle length also has a direct impact on the initial stiffness, the plastic stiffness, and the overall strength of the connection. As an example, comparing specimens DWA-16, and DWA-17 unveils that increasing web angle length from 120mm to 130 mm, increases the initial stiffness, and the plastic stiffness by 18%, and 22%, respectively, as is illustrated in Figure 54.

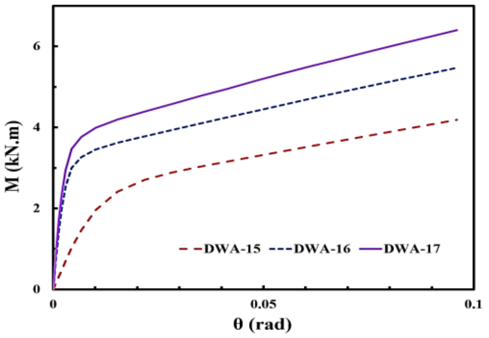

Fig. 54: Effects of web angle length on the performance of the connection.

5.1.3. Effects of web angle flange length

Opposite to previous sections, the web angle flange length has an inverse effect on the initial stiffness, the plastic stiffness, and the overall strength of the connection. As an example, increasing the web angle flange length in specimens DWA-26, DWA-27 from 80mm to 100mm, decreases the initial stiffness, and the plastic stiffness, by

40%, and 22%, respectively. This matter is shown in Figure 55.

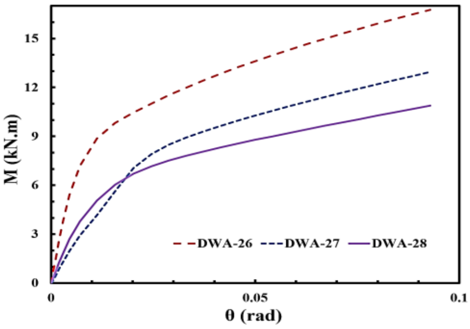

Fig. 55: Effects of web angle flange length on the performance of the connection.

5.2. *Welded flange plate connection*

The analytical and numerical results are presented in Table 5.

Similar to double web angle connections, Chisala's model precisely determines the values necessary to form the moment-rotation curve for welded flange plate connections as well. Using the collected data, analytical and numerical moment-rotation curves for some of the specimens were illustrated. These curves are shown in the figures 56 to 81:

Table 5: Analytical and numerical results for welded flange plate connection.

Specimen ID	K_i (kN.m/rad)		K_p (kN.m/rad)		M_0 (kN.m)	
	(Analytical)	(Abaqus)	(Analytical)	(Abaqus)	(Analytical)	(Abaqus)
MR-01	22352.600	21936.400	668.000	650.350	56.400	56.200
MR-02	22967.600	22637.920	683.200	671.180	57.200	57.000
MR-03	24071.500	23748.580	710.400	636.600	58.700	59.000
MR-04	25034.000	24681.030	733.900	726.540	60.100	62.000
MR-05	31303.100	29725.620	883.400	852.790	85.200	84.000
MR-06	33744.600	32168.540	940.300	917.600	89.500	89.100
MR-07	34415.700	33013.600	955.800	943.970	90.800	90.500
MR-08	35595.400	34468.370	982.900	979.320	93.200	93.000
MR-09	54913.100	50045.620	1408.600	1376.140	143.800	144.000
MR-10	55961.800	51430.660	1430.800	1407.860	145.900	145.000
MR-11	57801.600	53337.380	1469.800	1458.390	149.700	148.500
MR-12	59362.800	55244.360	1502.700	1507.270	153.200	151.000
MR-13	22352.600	21957.200	668.000	654.940	56.400	56.000
MR-14	22352.600	21964.700	668.000	654.270	56.400	55.500
MR-15	22352.600	21971.970	668.000	653.990	56.400	56.200
MR-16	29191.100	29412.790	833.700	844.990	84.300	83.500
MR-17	27346.100	29071.500	789.700	835.420	83.500	83.300
MR-18	25720.400	28593.960	750.500	821.170	82.900	83.100
MR-19	57801.600	50475.920	1469.800	1385.750	145.400	144.500
MR-20	56320.300	50287.300	1438.500	1380.680	144.600	144.300
MR-21	53574.400	49822.200	1380.000	1369.870	143.100	143.700
MR-22	21717.700	21745.130	652.200	647.780	55.400	55.500
MR-23	21014.200	21385.120	634.600	638.040	54.400	54.800
MR-24	20228.500	21033.540	614.900	628.850	53.400	54.000
MR-25	31625.700	29969.290	891.000	859.720	85.900	85.700
MR-26	31933.600	30167.340	898.200	866.040	86.600	86.500
MR-27	32227.900	30331.800	905.100	871.290	87.200	87.000
MR-28	55272.900	52849.840	1416.200	1378.420	144.700	145.500
MR-29	55619.200	56535.540	1423.600	1381.240	145.600	146.000
MR-30	55952.600	57672.600	1430.700	1384.569	146.400	144.800
MR-31	23359.900	23357.660	692.900	691.130	58.200	58.700
MR-32	24083.400	24382.580	710.700	716.110	59.700	60.400
MR-33	24853.100	25774.880	729.500	753.090	61.600	62.000
MR-34	32983.600	31649.000	922.600	906.190	87.400	87.000
MR-35	34854.800	33347.950	965.900	951.890	90.200	89.600
MR-36	35356.200	34062.470	977.400	973.400	91.000	90.500
MR-37	58244.700	52849.840	1479.100	1447.280	147.600	147.000
MR-38	62006.800	56535.540	1558.000	1540.570	152.200	151.000
MR-39	63024.500	57672.600	1579.200	1569.520	153.600	152.000
MR-40	22352.600	21958.960	668.000	651.010	56.400	56.200

MR-41	22352.600	21957.610	668.000	650.960	56.400	56.200
MR-42	22352.600	21953.120	668.000	650.860	56.400	56.200
MR-43	22352.600	22355.910	668.000	661.430	57.700	56.800
MR-44	22352.600	22638.620	668.000	668.890	58.800	57.800
MR-45	22352.600	22831.880	668.000	674.310	59.900	58.300
MR-46	31303.100	30162.650	883.400	865.870	85.900	85.100
MR-47	31303.100	30582.440	883.400	875.730	86.500	85.500
MR-48	31303.100	30941.570	883.400	887.060	87.100	86.000
MR-49	54913.100	50580.290	1408.600	1385.80	144.700	144.200
MR-50	54913.100	50749.300	1408.600	1387.470	145.600	144.500
MR-51	54913.100	50902.060	1408.600	1397.030	147.300	145.300
MR-52	22352.600	21991.420	668.000	651.900	56.400	56.200
MR-53	22352.600	22033.220	668.000	653.340	56.400	56.200
MR-54	22352.600	22107.500	668.000	655.390	56.400	56.200
MR-55	22352.600	21916.280	668.000	649.910	56.400	56.200
MR-56	22352.600	21974.890	668.000	651.630	56.400	56.200
MR-57	22352.600	22073.280	668.000	654.190	56.400	56.200
MR-58	22352.600	21951.160	668.000	650.830	56.400	56.200
MR-59	22352.600	21915.000	668.000	649.850	56.400	57.500
MR-60	22352.600	21902.510	668.000	649.510	56.400	58.000
MR-61	22352.600	22349.030	668.000	661.210	56.900	56.700
MR-62	22352.600	22691.730	668.000	672.420	57.300	57.300
MR-63	22352.600	22914.900	668.000	680.800	57.500	57.500
MR-64	31303.100	30151.410	883.400	866.040	85.900	85.500
MR-65	31303.100	30621.460	883.400	877.890	86.500	86.000
MR-66	31303.100	31052.860	883.400	890.860	86.900	86.500
MR-67	54913.100	50721.680	1408.600	1393.500	145.000	145.000
MR-68	54913.100	51202.700	1408.600	1407.980	145.900	146.000
MR-69	54913.100	53195.710	1408.600	1463.270	146.700	148.500
MR-70	23587.400	22975.170	698.500	688.560	58.100	57.000
MR-71	24597.800	24336.970	723.200	734.300	59.500	57.500
MR-72	25439.900	25547.900	743.700	775.390	60.800	58.000
MR-73	33327.400	31639.690	930.600	1003.730	88.400	91.500
MR-74	34886.600	33505.580	966.600	1058.720	91.100	91.700
MR-75	36124.400	34614.470	995.000	1107.050	93.500	92.000
MR-76	58616.400	53564.010	1487.000	1484.730	149.000	157.000
MR-77	61517.300	56669.330	1547.800	1577.540	153.400	158.500
MR-78	63851.200	60988.610	1596.400	1714.760	157.300	160.500

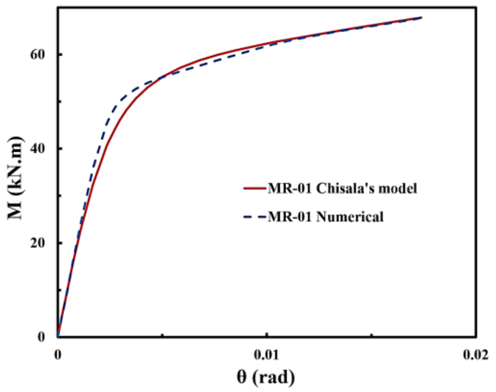

Fig. 56: Numerical and analytical moment-rotation curves for MR-01 specimen.

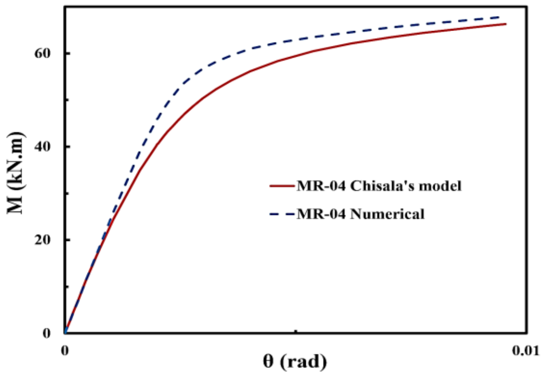

Fig. 57: Numerical and analytical moment-rotation curves for MR-04 specimen.

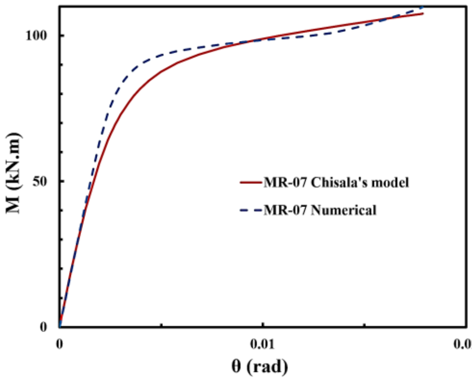

Fig. 58: Numerical and analytical moment-rotation curves for MR-07 specimen.

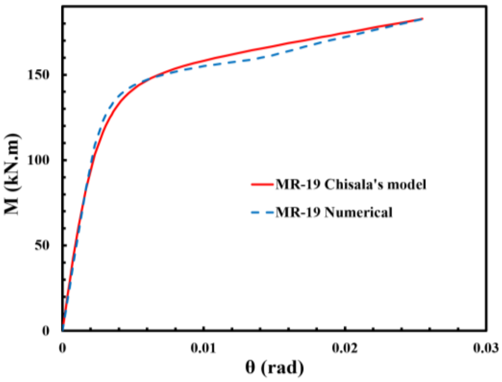

Fig. 62: Numerical and analytical moment-rotation curves for MR-19 specimen.

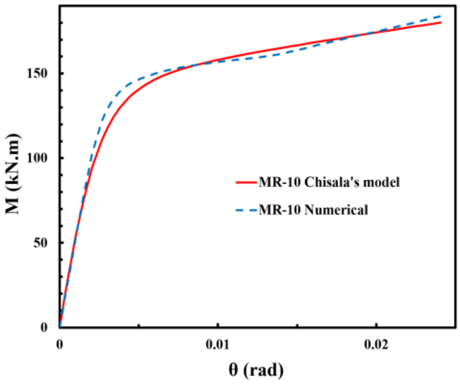

Fig. 59: Numerical and analytical moment-rotation curves for MR-10 specimen.

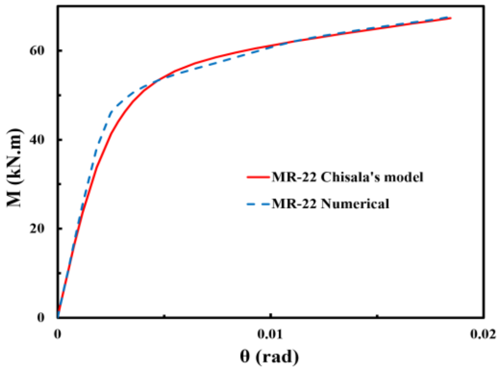

Fig. 63: Numerical and analytical moment-rotation curves for MR-22 specimen.

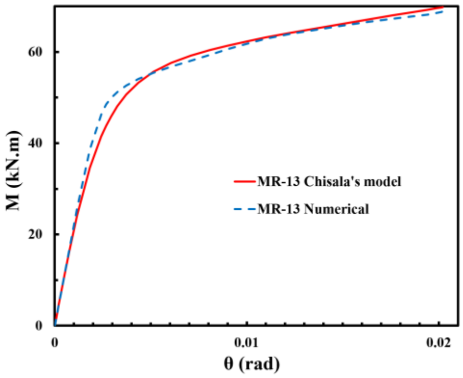

Fig. 60: Numerical and analytical moment-rotation curves for MR-13 specimen.

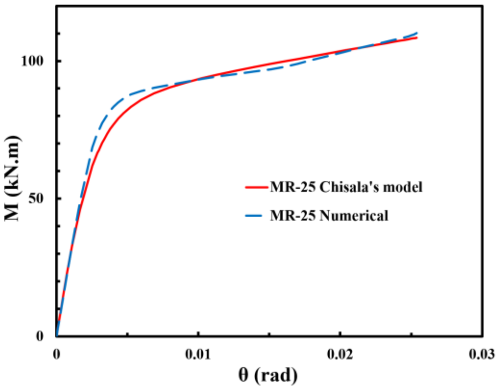

Fig. 64: Numerical and analytical moment-rotation curves for MR-25 specimen.

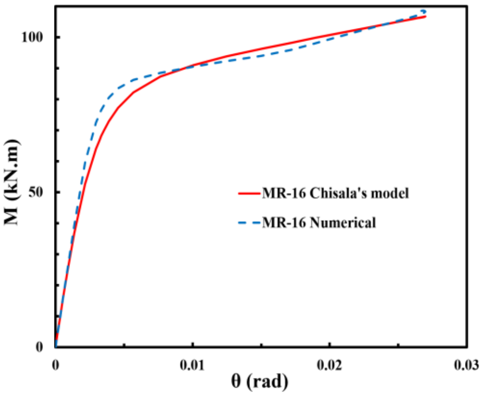

Fig. 61: Numerical and analytical moment-rotation curves for MR-16 specimen.

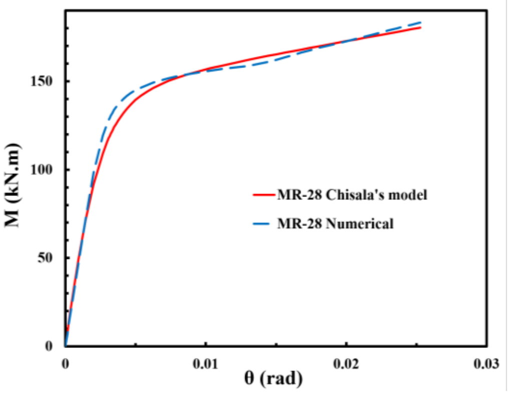

Fig. 65: Numerical and analytical moment-rotation curves for MR-28 specimen.

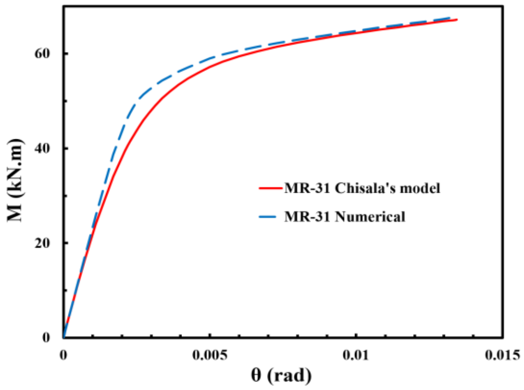

Fig. 66: Numerical and analytical moment-rotation curves for MR-31 specimen.

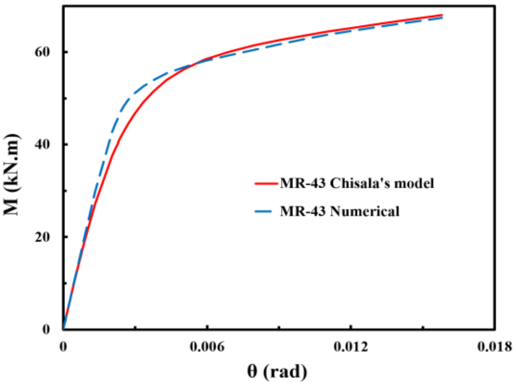

Fig. 70: Numerical and analytical moment-rotation curves for MR-43 specimen.

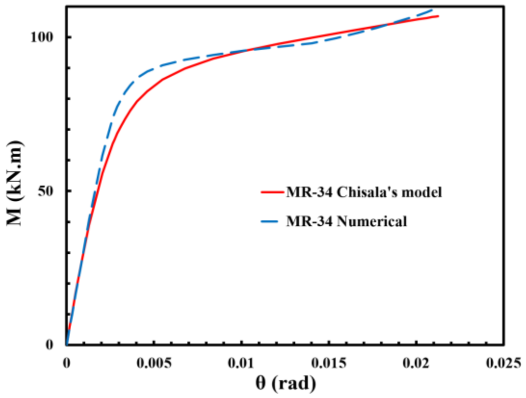

Fig. 67: Numerical and analytical moment-rotation curves for MR-34 specimen.

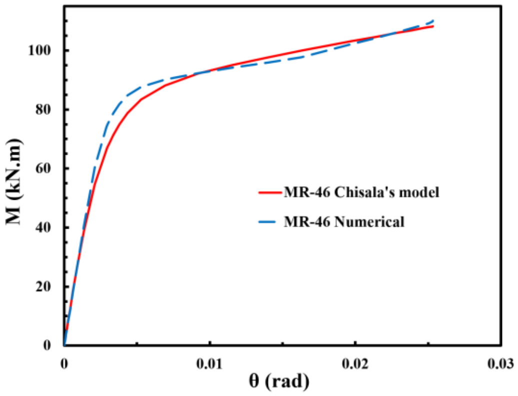

Fig. 71: Numerical and analytical moment-rotation curves for MR-46 specimen.

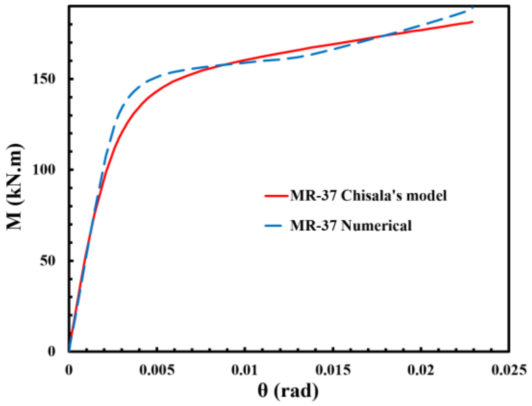

Fig. 68: Numerical and analytical moment-rotation curves for MR-37 specimen.

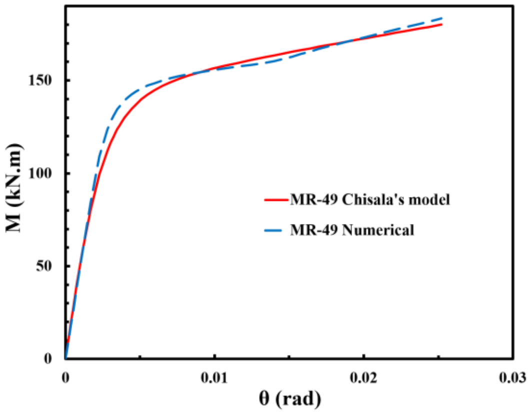

Fig. 72: Numerical and analytical moment-rotation curves for MR-49 specimen.

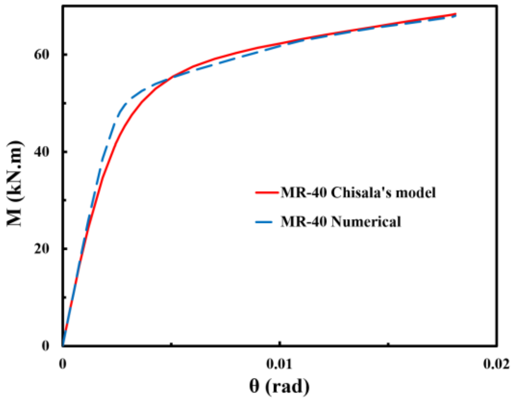

Fig. 69: Numerical and analytical moment-rotation curves for MR-40 specimen.

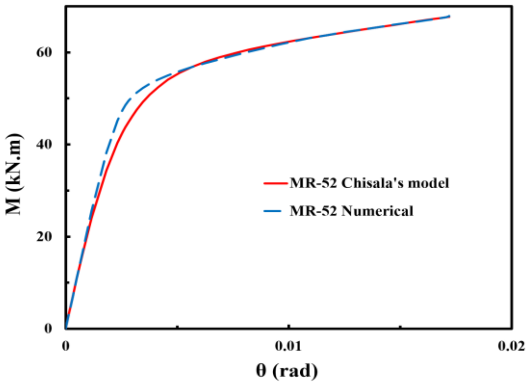

Fig. 73: Numerical and analytical moment-rotation curves for MR-52 specimen.

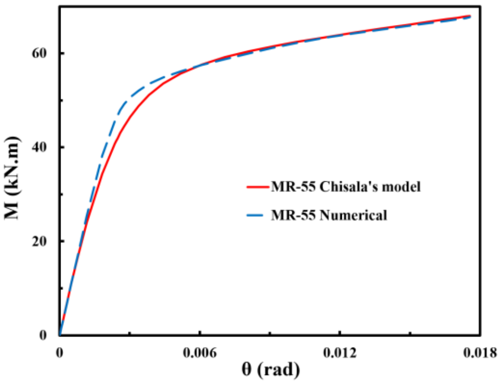

Fig. 74: Numerical and analytical moment-rotation curves for MR-55 specimen.

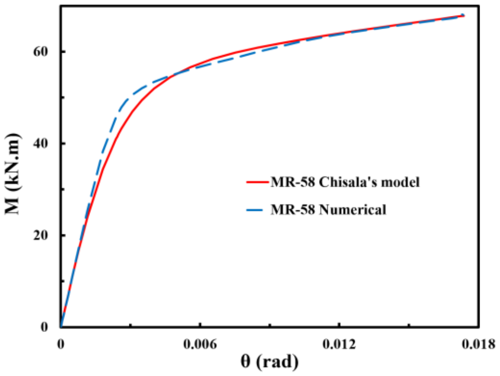

Fig. 75: Numerical and analytical moment-rotation curves for MR-58 specimen.

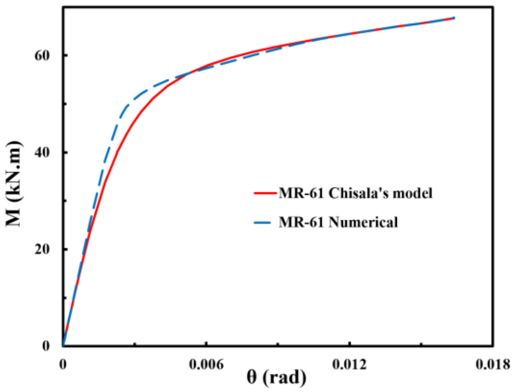

Fig. 76: Numerical and analytical moment-rotation curves for MR-61 specimen.

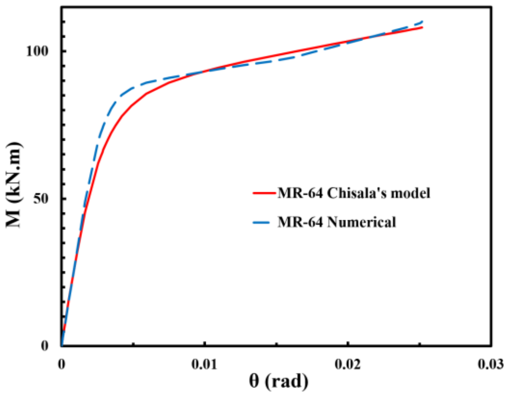

Fig. 77: Numerical and analytical moment-rotation curves for MR-64 specimen.

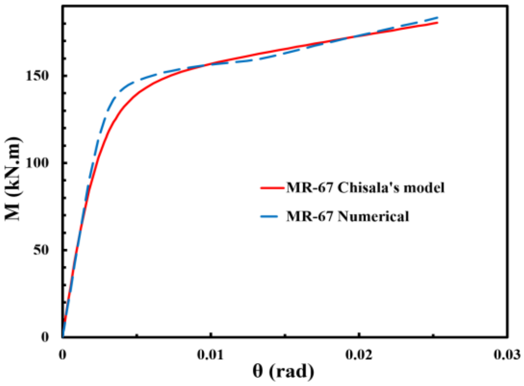

Fig. 78: Numerical and analytical moment-rotation curves for MR-67 specimen.

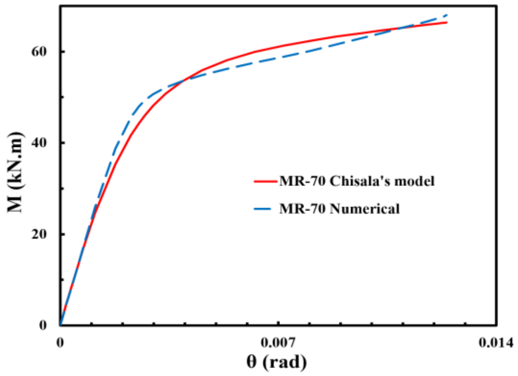

Fig. 79: Numerical and analytical moment-rotation curves for MR-70 specimen.

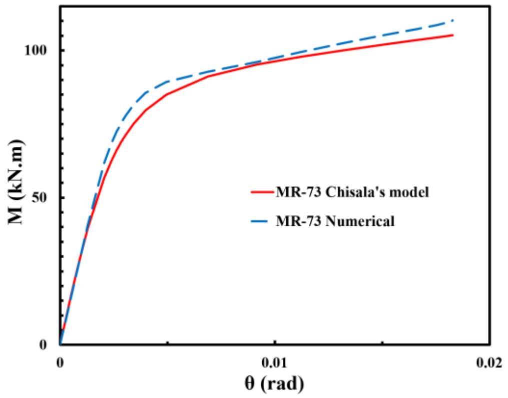

Fig. 80: Numerical and analytical moment-rotation curves for MR-73 specimen.

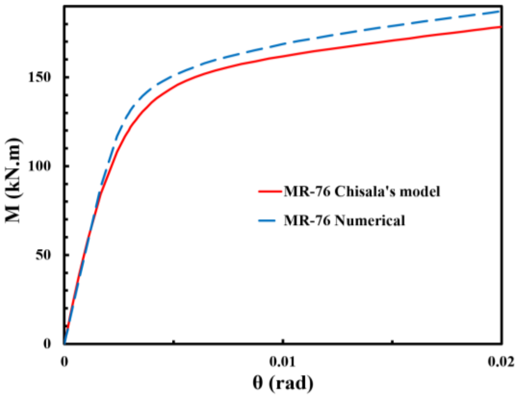

Fig. 81: Numerical and analytical moment-rotation curves for MR-76 specimen.

There are some other results obtained from the data, which are described in the following sections.

5.2.1. *Effects of top plate thickness, width, and length*

Comparing the obtained results, it appears that the thickness and the width of the top plate have a direct and significant effect on the stiffness (both elastic and plastic), and the overall strength of the connection. Increasing the length of the welded zone does not affect the performance of the connection very much, although increasing the dimensions of the trapezoid part has an inverse effect on the stiffness and the overall strength of the connection. These differences are not quite visible in Figure 82., Figure 83., and Figure 84., mainly because of insignificant changes of dimensions, due to design code limitations.

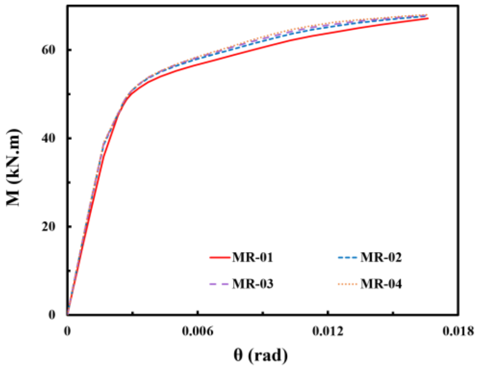

Fig. 82: Effects of top plate thickness on the performance of the connection.

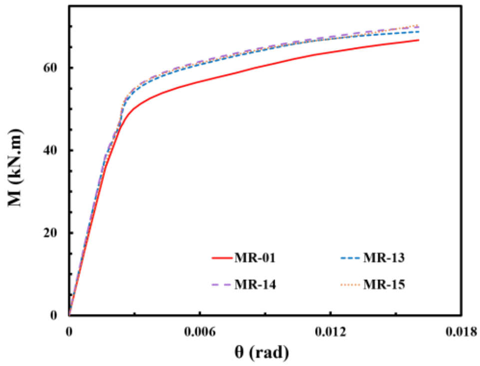

Fig. 83: Effects of top plate length on the performance of the connection.

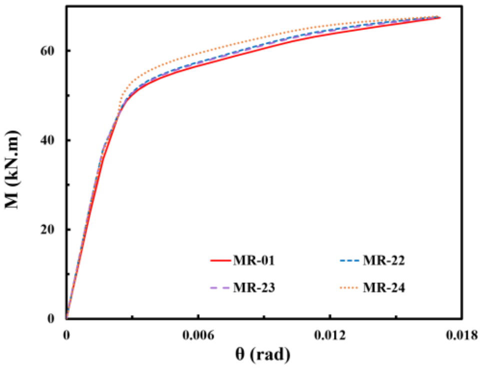

Fig. 84: Effects of top plate width on the performance of the connection.

5.2.2. *Effects of bottom plate thickness, width, and length*

As illustrated in Figure 85., Figure 86., and Figure 87., this section is similar to the previous, which was predictable.

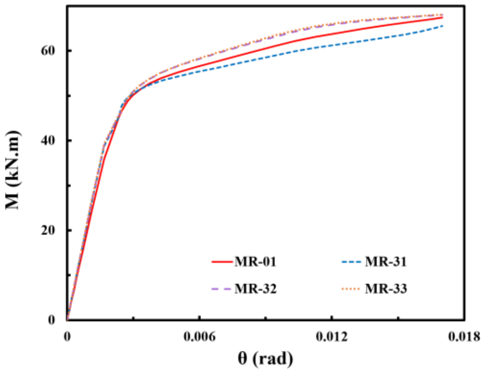

Fig. 85: Effects of bottom plate thickness on the performance of the connection.

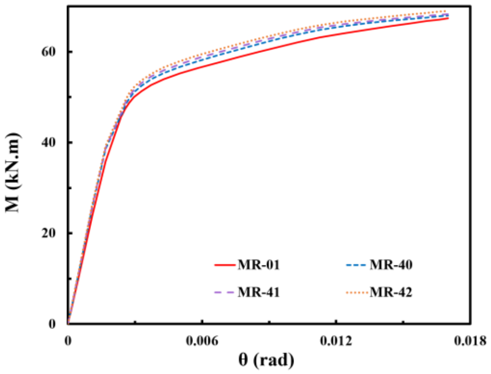

Fig. 86: Effects of bottom plate length on the performance of the connection.

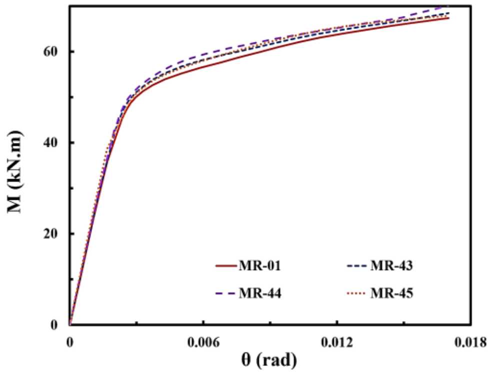

Fig. 87: Effects of bottom plate width on the performance of the connection.

5.2.3. *Effects of beam web stiffener thickness, width, and length*

The length and the thickness of the beam web stiffener, since it is welded to the beam web on all edges, do not affect the moment-rotation curve significantly. As for the width, most of the flexural moment is transferred to the column, through tensile, and compressive couple forces generated in the top and bottom plates, therefore, the width of the beam web stiffener does not significantly alter the performance of the connection.

5.2.4. *Effects of continuity plate thickness*

Continuity plate will prevent local buckling of the column flanges. Increasing its thickness leads to increased stiffness and the overall strength of the connection, as shown in Figure 88.

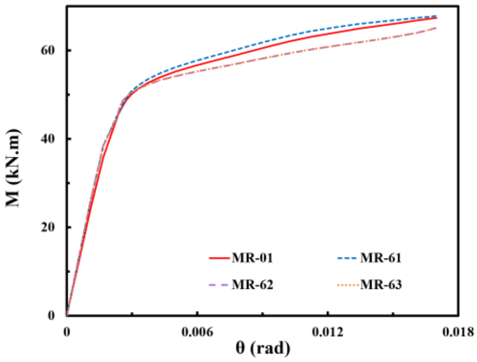

Fig. 88. Effects of continuity plate thickness on the performance of the connection.

5.2.5. *Effects of doubler plates thickness (column web stiffener plate)*

Changing the thickness of doubler plates has a direct effect on the stiffness and the overall strength of the connection, as it stiffens the panel zone against flexural-moment. This is shown in Figure 89.

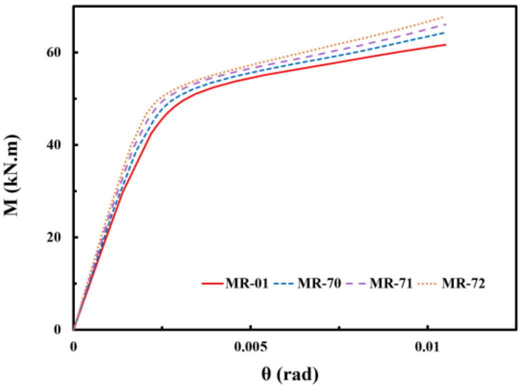

Fig. 89. Effects of doubler plate thickness on the performance of the connection.

6. Conclusions

To determine the efficiency of Chisala's model in predicting the moment-rotation curve for double web angle, and welded flange plate connections, analytical and numerical models were made, and using both, the parameters needed to construct the moment-rotation curve were calculated. Based on the results, the following conclusions are made:

1- Utilized finite element models and the choice of materials are reliable.

2- Compared to other models, Chisala's model is more efficient in predicting the moment-rotation curve for different types of steel connections, since it has fewer parameters, and these parameters are independent.

3- Chisala's model can precisely predict the moment-rotation curve for double web angle, and welded flange plate connections.

4- Since the precision of Chisala's model is acceptable, further research on the performance of different types of steel connections using this model is recommended.

5- As Chisala's model is expressed in a general form, constructing a proper equivalent analytical model to determine the parameters, is the key step while employing the model.

6- The equivalent analytical model can be constructed using the basics of structural analysis, and a system formed by a combination of different springs, each resembling the stiffness of a different part of the whole connection.

7- Since the plastic stiffness is expressed in terms of the initial stiffness, linear springs can form the equivalent analytical model, which simplifies the analysis significantly.

8- Geometric dimensions do affect the flexural performance of double web angle and welded flange plate connections. In this regard, the thickness, and flange length of the web angle, in double web angle connections, and the dimensions of the bottom plate, in welded flange plate connections, seem to have the most noticeable impacts on the performance of these connections.

9- The nonlinear performance of double web angle connections begins in connecting elements (welding and angle sections) whereas in the welded flange plate connections, it begins in beams and then extends to the whole connection.

10- The very two types of connections exhibit a semi-rigid flexural performance.

Acknowledgments

Authors did not receive any financial support for the research, authorship, and publication of this project.

References

[1] R.M. Richard, W.-k. Hsia, M. Chmielowiec, Derived moment rotation curves for double framing angles, Computers & Structures 30(3) (1988) 485-494.

[2] C.W. Lewitt, W.H. Munse, E. Chesson, Restraint characteristics of flexible riveted and bolted beam-to-column connections, University of Illinois. Engineering Experiment Station. Bulletin ; No. 500, 1969.

[3] M.J. Frye, G.A. Morris, Analysis of flexibly connected steel frames, Canadian Journal of Civil Engineering 2(3) (1975) 280-291.

[4] R.M. Richard, B.J. Abbott, Versatile elastic-plastic stress-strain formula, Journal of the Engineering Mechanics Division 101(4) (1975) 511-515.

[5] K.M. Ang, G.A. Morris, Analysis of three-dimensional frames with flexible beam–column connections, Canadian Journal of Civil Engineering 11(2) (1984) 245-254.

[6] E. Attiogbe, G. Morris, Moment-rotation functions for steel connections, Journal of Structural Engineering 117(6) (1991) 1703-1718.

[7] N. Kishi, M. Komuro, W.F. Chen, Four-parameter power model for M-θ curves of end-plate connections, Proceedings of connection in steel structures V. Amsterdam (2004) 99-110.

[8] A. Abolmaali, J.H. Matthys, M. Farooqi, Y. Choi, Development of moment–rotation model equations for flush end-plate connections, Journal of Constructional Steel Research 61(12) (2005) 1595-1612.

[9] V.L. Tran, Moment-rotation-temperature model of semi-rigid cruciform flush endplate connection in fire, Fire Safety Journal 114 (2020) 102992.

[10] M.L. Chisala, Modelling M–φ curves for standard beam-to-column connections, Engineering Structures 21(12) (1999) 1066-1075.

[11] F.H.S. Gilio, L.C.M. Vieira, M. Malite, Stability and moment-rotation behavior of cold-formed steel purlins with sleeved bolted connection, Engineering Structures 171 (2018) 658-672.

[12] G. Zhou, Y. An, Z. Wu, D. Li, J. Ou, Analytical model for initial rotational stiffness of steel beam to concrete-filled steel tube column connections with bidirectional bolts, Journal of Structural Engineering 144(11) (2018) 04018199.

[13] B. Zhao, C. Sun, H. Li, Study on the moment-rotation behavior of eccentric rectangular hollow section cross-type connections under out-of-plane bending moment and chord stress, Engineering Structures 207 (2020) 110211.

[14] S.S. Lee, T.S. Moon, Moment–rotation model of semi-rigid connections with angles, Engineering Structures 24(2) (2002) 227-237.

[15] Z. Kong, S.-E. Kim, Moment-rotation behavior of top- and seat-angle connections with double web angles, Journal of Constructional Steel Research 128 (2017) 428-439.

[16] F. Danesh, A. Pirmoz, A.S. Daryan, Effect of shear force on the initial stiffness of top and seat angle connections with double web angles, Journal of Constructional Steel Research 63(9) (2007) 1208-1218.

[17] M. Mofid, M.R.S. Mohammadi, S.L. McCabe, Analytical approach on endplate connection: ultimate and yielding moment, Journal of Structural Engineering 131(3) (2005) 449-456.

[18] M.S. Ghobadi, A. Mazroi, M. Ghassemieh, Cyclic response characteristics of retrofitted moment resisting connections, Journal of Constructional Steel Research 65(3) (2009) 586-598.

[19] E.C.F. STANDARDIZATION, Eurocode 3, Design of steel structures - Part 1-8: Design of joints, Brussels, 2003.

[20] J.G. Yang, G.Y. Lee, Analytical models for the initial stiffness and ultimate moment of a double angle connection, Engineering Structures 29(4) (2007) 542-551.

[21] R. Szilard, Theories and applications of plate analysis: classical, numerical and engineering methods, John Wiley & Sons, Inc.2004.

[22] K.D. Kim, M.D. Engelhardt, Monotonic and cyclic loading models for panel zones in steel moment frames, Journal of Constructional Steel Research 58(5) (2002) 605-635.

[23] G. Brandonisio, A. De Luca, E. Mele, Shear strength of panel zone in beam-to-column connections, Journal of Constructional Steel Research 71 (2012) 129-142.